sustainability

MDPI

Article

Infiltration Efficiency Index for GIS Analysis Using Very-High-Spatial-Resolution Data

Ante Šiljeg [1], Lovre Panđa [1,*], Rajko Marinović [1], Nino Krvavica [2], Fran Domazetović [1], Mladen Jurišić [3] and Dorijan Radočaj [3]

[1] Department of Geography, University of Zadar, 23000 Zadar, Croatia; asiljeg@unizd.hr (A.Š.); rmarinovi22@unizd.hr (R.M.); fdomazeto@unizd.hr (F.D.)
[2] Faculty of Civil Engineering, University of Rijeka, 51000 Rijeka, Croatia; nino.krvavica@gradri.uniri.hr
[3] Faculty of Agrobiotechnical Sciences, Josip Juraj Strossmayer University of Osijek, 31000 Osijek, Croatia; mladen.jurisic@fazos.hr (M.J.); dradocaj@fazos.hr (D.R.)
* Correspondence: lpanda@unizd.hr

Abstract: Infiltration models and impervious surface models have gained significant attention in recent years as crucial tools in urban and environmental planning, to assess the extent of land-surface changes and their impacts on hydrological processes. These models are important for understanding the hydrological dynamics and ecological impacts of urbanization and for the improvement of sustainable land-use planning and stormwater-management strategies. Due to the fact that many authors partially or entirely overlook the significance of the infiltration process in geographic information system (GIS) analyses, there is currently no universally accepted method for creating an infiltration model that is suitable for GIS multicriteria decision analysis (GIS-MCDA). This research paper presents an innovative approach to modeling the infiltration-efficiency index (IEI) for GIS analysis, with a focus on achieving high-quality results. The proposed methodology integrates very-high-resolution (VHR) remote-sensing data, GIS-MCDA, and statistical methods. The methodology was tested and demonstrated on a small sub-catchment in Metković, Croatia. The study developed a VHR IEI model from six specific criteria that produced values between 0 and 0.71. The model revealed that 14.89% of the research area is covered by impervious surfaces. This percentage is relatively favorable when compared to urban areas globally. The majority of the research area (62.79%) has good infiltration efficiency. These areas are predominantly characterized by agricultural land use, encompassing orchards, tangerines, olive groves, vineyards, and a diverse range of low-lying and high vegetation on flat terrain. The IEI model can provide input spatial data for high-resolution GIS analysis of hydrological processes. This model will aid decision-makers in stormwater-management, flood-risk assessment, land-use planning, and the design of green infrastructure. By utilizing the information derived from this study, policymakers can make informed decisions to mitigate flooding risks and promote sustainable urban development.

Keywords: imperviousness; infiltration; efficiency; GIS-MCDA; UAV; multispectral imagery; LiDAR; very-high-resolution; Metković; Croatia

check for updates

Citation: Šiljeg, A.; Panđa, L.; Marinović, R.; Krvavica, N.; Domazetović, F.; Jurišić, M.; Radočaj, D. Infiltration Efficiency Index for GIS Analysis Using Very-High-Spatial-Resolution Data. *Sustainability* **2023**, *15*, 15563. https://doi.org/10.3390/su152115563

Academic Editor: Vilém Pechanec

Received: 3 October 2023
Revised: 27 October 2023
Accepted: 31 October 2023
Published: 2 November 2023

Copyright: © 2023 by the authors. Licensee MDPI, Basel, Switzerland. This article is an open access article distributed under the terms and conditions of the Creative Commons Attribution (CC BY) license (https://creativecommons.org/licenses/by/4.0/).

1. Introduction

Impervious surfaces (ISs), such as roads, parking lots, rooftops, and sidewalks, are anthropogenic features that restrict the natural infiltration of rainwater into the ground, leading to increased stormwater runoff and altered hydrological dynamics in urban areas [1,2]. With rapid urbanization leading to increased imperviousness, as well as climate-change disruptions in the precipitation regime and its associated impacts [3,4], accurate and high-resolution IS modeling is crucial for assessing the extent of ISs and evaluating stormwater runoff and flooding risks [5,6]. Infiltration is another significant process in hydrology and environmental science; it refers to the vertical movement of water from the surface into the subsurface soil or rock layers in pervious surfaces [7]. Understanding and managing infiltration processes are vital for sustainable water-resource management and ecosystem functioning.

Impervious-surface models, infiltration-capacity models, and infiltration-rate models are important for understanding the hydrological dynamics and ecological impacts of urbanization on the improvement of sustainable land-use planning and on stormwater-management strategies [8,9].

Urban and environmental planners rely on different data sources to quantify and map the spatial distribution of ISs, assess the ecological and hydrological impacts of imperviousness, and make informed decisions related to stormwater management, land-use planning, and green infrastructure design [10]. High-resolution IS models and infiltration models provide detailed and accurate information on hydrologic processes within urban areas [11], allowing for a better understanding of stormwater runoff, flood risks, and water-quality impacts [1,12–16].

IS modeling has progressed significantly in recent years, with numerous studies exploring different approaches and methods for accurately estimating and mapping ISs in urban areas. Generally, methods of IS modeling can be divided into four main categories: (1) spectral indices [17–19], (2) spectral-mixture analysis [20–22], (3) regression models [23,24], and (4) machine-learning methods [25–27].

The methods and approaches employed in IS modeling are continuously advancing and refining, as evidenced by the ever-growing body of scientific literature and the development of novel techniques and technologies that are aimed at enhancing the accuracy, resolution, and applicability of IS models.

Among the various imperviousness models available, the 10 m spatial resolution imperviousness density model provided by the European Union's Earth observation program, Copernicus, is widely recognized and commonly employed for urban and environmental planning purposes [28–31]. This model utilizes satellite imagery and advanced remote-sensing techniques to accurately capture and quantify ISs at a spatial resolution of 10 m [32]. This Copernicus "high-resolution" imperviousness density model shows the degree of soil sealing. The imperviousness gradation (0–100%) for each pixel is calculated based on the calibrated normalized difference vegetation index (NDVI) and semi-automated classification. The term "soil sealing" is used because the transformation of natural surfaces with paved roads, concrete surfaces, buildings, and other infrastructure occurs, thereby creating impervious land cover. With that process, natural surfaces are separated from the atmosphere by impermeable layers [32].

Infiltration is commonly modeled or computed using various approaches in hydrological science, which vary with respect to the type of land-cover (LC) class [33–36]. One widely used method is the natural resources conservation service (NRCS) method, which uses curve numbers (CN) to estimate infiltration rates [37–39]. The CN values are assigned on the basis of land use and soil group, enabling the estimations of runoff and infiltration for different conditions [37]. Another approach is the Horton equation, which describes infiltration as a decaying exponential function over time, taking into account parameters such as initial infiltration rate and hydraulic conductivity [40]. Finally, the Green–Ampt model is frequently employed, especially for intense rainfall events, as it incorporates soil properties, initial moisture content, and hydraulic conductivity to estimate infiltration rates and cumulative infiltration [41].

However, it is important to note that, while these infiltration models provide valuable insights, they often neglect or only partially account for surface conditions that can significantly impact infiltration rates [42]. Factors such as soil surface sealing, vegetation cover, surface roughness, and antecedent moisture conditions are not always adequately considered [33,35,43–47]. Consequently, these models may not accurately capture the complex interactions between surface characteristics and infiltration processes [34].

Given the rapid development of geospatial technologies (GSTs), there is a need for integrated imperviousness and infiltration models that incorporate more detailed and precise information. By using higher-resolution data and advanced analysis techniques, and by integrating infiltration models with imperviousness models, these models can provide more accurate and comprehensive assessments of ISs and infiltration, thereby enhancing their utility in sustainable urban and environmental planning and policymaking.

However, modeling ISs and infiltration using high-spatial-resolution data can be affected by several challenges, including data availability, data accuracy, and processing methods. Remote-sensing techniques, such as satellite imagery and light detection and ranging (LiDAR), have been widely used, but the accuracy and resolution of these datasets can vary [2,45,48–50]. Additionally, the complex spectral nature of urban areas, such as varying building types (resulting in large shadows), surface materials, and land-use patterns, pose challenges in developing accurate high-resolution models [2,45,48–50]. For these reasons, it is necessary to manually correct the produced models [51,52].

Many authors engage in flood-susceptibility modeling, but to date, no one has utilized infiltration as an input criterion for geographic information system (GIS) multicriteria decision analysis (GIS-MCDA) [53–56]. This research paper aims to address this challenge by proposing a new approach to high-quality infiltration modeling that integrates a cluster of criteria, including both IS criteria and infiltration-capacity criteria into a single criterion called the infiltration-efficiency index (IEI). This criterion is expressed as a nondimensional index, which is more suitable for GIS analysis in comparison to physical models, such as the NRCS-CN, Horton, or Green–Ampt methods. Most researchers investigating this topic have concentrated their efforts on the examination of infiltration efficiency within urban drainage systems [57–60]. However, similar studies are needed also for large-scale analysis where the study area encompasses an entire city or catchment, rather than just focusing on specific location points. The purpose of this study is to utilize various parameters to elucidate disparities in infiltration efficiency within urban areas and to develop a model that provides spatial input data to GIS spatial analyses. The proposed IEI is built upon CN numbers, but also includes additional parameters that are not considered under the conventional NRCS method, such as slope, vegetation health (NDVI), wetness, and temperature.

This approach integrates very-high-resolution (VHR) remote-sensing data, GIS-MCDA, and statistical methods to determine land-surface impermeability and surface conditions that are crucial for stormwater-runoff risk management. The research explores different data sources, such as VHR multispectral imagery and LiDAR data. Furthermore, different land-use and land-cover (LULC) classification methods and model-validation approaches are examined to develop a robust and accurate infiltration model that includes imperviousness criteria, which will be enhanced by the inclusion of various spatial criteria through the GIS-MCDA process.

The results of this research will contribute to the advancement of VHR impervious-surface and infiltration modeling and provide valuable insights for urban and environmental planners to better understand the impacts of various spatial criteria on overall infiltration efficiency and encourage sustainable urban planning practices.

2. Materials and Methods

2.1. Study Area

Metković is a Croatian city located in the southern part of the country (Figure 1A), with a population of 15,235 inhabitants, according to the latest available census data [61]. The northwestern part of the city (1.64 km^2), located on the right bank of the Neretva River (Figure 1B), was selected as a study area, due to its unique geographical, climatological, and ecological features. The selection of this specific area was driven by the complexity and diversity of land use (including agriculture and urban areas). as well as by its susceptibility to flooding. In the context of the Interreg Strategic Development of Flood Management (STREAM) project, the authors undertook an extensive modeling effort aimed at pluvial-flood analysis, which was conducted on a much wider area and across multiple scales. Interestingly, this part of the city emerged as one of the most susceptible to pluvial flooding. Consequently, it was strategically chosen as a micro-level research area, based primarily on the substantial volume of data and the requisite level of detail necessary for the study's objectives [62]. Due to the lowland nature of the area and its proximity to a major river, the region exhibits swampy characteristics that have fostered significant biodiversity. To facilitate economic development in the region, land-reclamation efforts were undertaken in the second half of the 20th century [63]. The soil in this wider area is predominantly alluvial, resulting from the accumulation of sediment and organic matter deposited by the river [63,64]. The alluvial soil is fertile and supports a variety of crops, making the area an essential agricultural region. Moreover, the area is intersected by irrigation channels, which provide efficient means of water distribution for crop cultivation. These channels contribute significantly to soil fertility and provide a sustainable source of water for agricultural purposes [63].

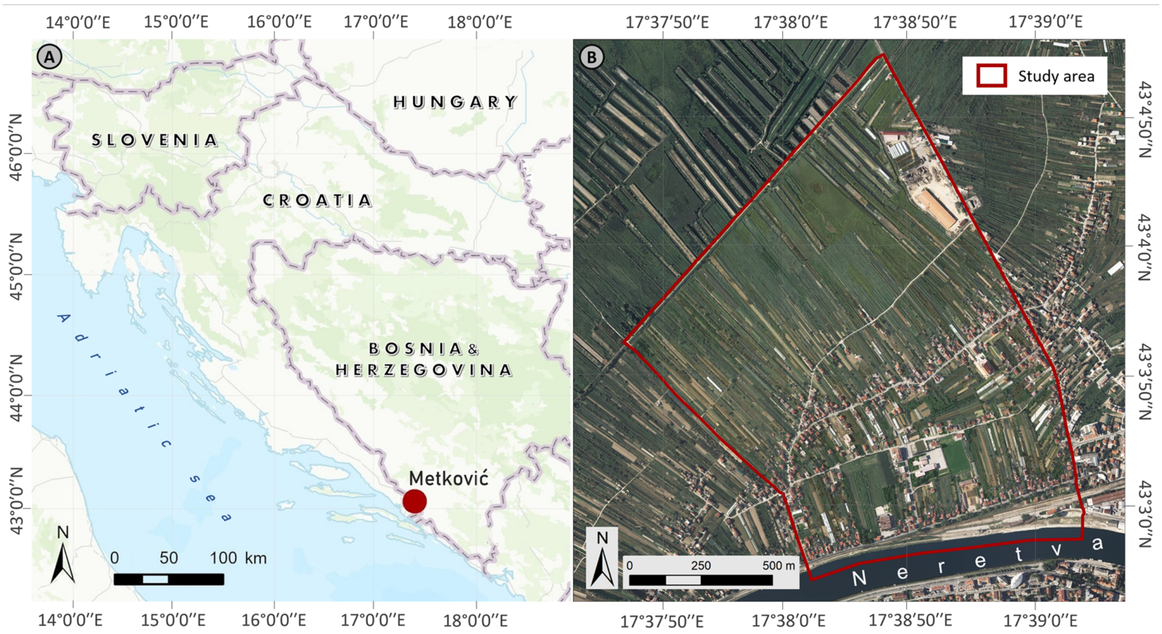

Figure 1. Geographical position of the study area: (**A**) In Croatia; (**B**) In the city of Metković.

Apart from agricultural activities, the study area contains a residential zone and some industrial facilities in its southern part. These objects represent the majority of ISs. In many cases, people added substantial amounts of material to elevate their homes above the surrounding terrain, creating basins that impede the outflow of water. These practices can cause water accumulation and flooding in this particular area.

Metković exhibits a Mediterranean climate that is characterized by hot and dry summers, mild and wet winters, and a pronounced seasonal variation in precipitation. The lowest monthly rainfall is in July and the highest monthly rainfall is in November. The average annual precipitation varies between 1125 mm and 1215 mm, with a median of 1162 mm [65].

2.2. The Research Methodology

The research methodology consisted of the following steps: (1) very-high-resolution data acquisition; (2) data processing; (3) creation of criteria; and (4) GIS-MCDA (Figure 2).

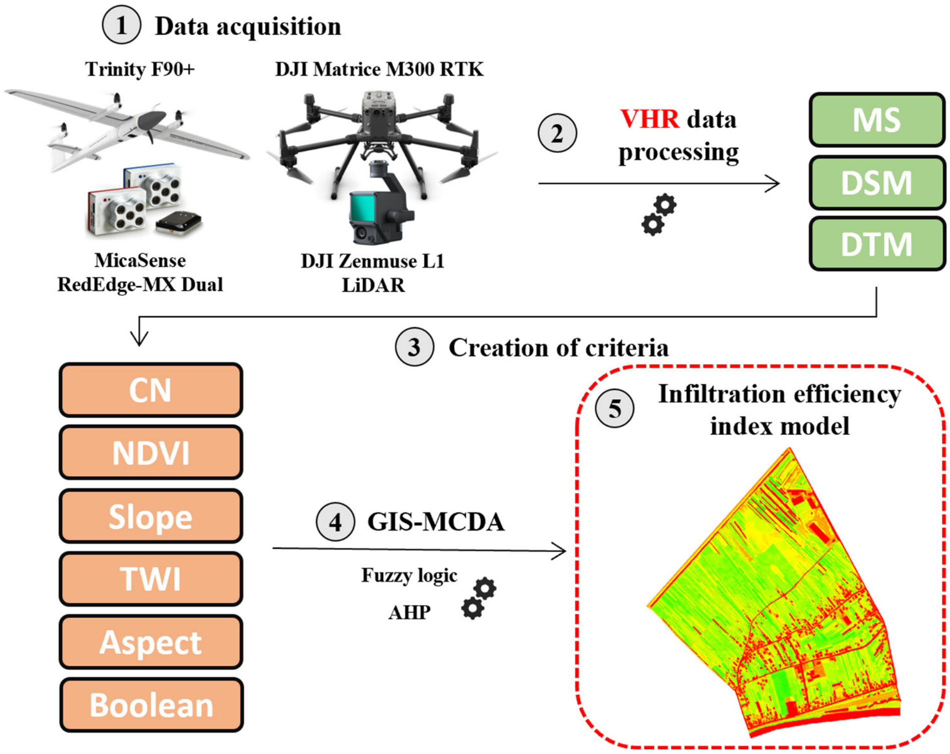

Figure 2. The methodological framework of the research: (**1**) Data acquisition; (**2**) VHR data processing; (**3**) Creation of criteria; (**4**) GIS-MCDA; (**5**) Infiltration efficiency index model.

2.3. Data Acquisition

2.3.1. UAV Multispectral Survey

The field research was conducted from 9 August 2022 to 13 August 2022. The first step involved an unmanned aerial vehicle (UAV) survey of Metković, using a dual multispectral camera system (MicaSense RedEdge-MX Dual MS) (Table 1). The sensor was integrated into the Trinity F90+ UAV, which offers exceptional imaging and data collection capabilities for recording vast and inaccessible areas [66]. The data were collected using the direct georeferencing method, which involves the integration of global mobile satellite system (GNSS) data and inertial measurement unit (IMU) data to accurately determine the position and orientation of the sensor platform during data acquisition. The RTK GNSS Trimble R12i was used to acquire checkpoints (CPs) and to establish a base point (BP).

Table 1. MicaSense RedEdge-MX Dual MS specifications [67].

Sensor type	Multispectral (MS)
Spectral bands	coastal blue (444 nm), blue (475 nm), green (531 nm), green (560 nm), red (650 nm), red (668 nm), red edge (705 nm), red edge (717 nm), red edge (740 nm), near-infrared (842 nm)
Ground sample distance	8 cm per pixel (per band) at 120 m

Before the UAV flight mission, CPs were collected to assess the accuracy of the UAV's direct georeferencing system. Additionally, the base point (BP) for the UAV's iBase base station was established (Figure 3A). The Croatian Terrestrial Reference System (HTRS96/TM) official projection coordinate system was employed to measure each point accurately. Subsequently, the planning of the UAV missions was conducted using the QBase 3D v2.30.77 software, considering factors such as the terrain morphology, the desired level of detail, and the relative flight time.

Figure 3. (**A**) CPs and BP collecting; (**B**) MS sensor calibrating; (**C**) Trinity F90+ filed survey.

For the multispectral (MS) imaging mission, a front overlap of 75% and a side overlap of 70% were chosen, considering the required level of detail. The UAV_{MS} settings and a flight altitude of 120 m resulted in a ground-sampling distance (GSD) of 8.33 cm/px. Before takeoff, the UAV's initial measurement unit (IMU) and compass were calibrated. Furthermore, the radiometric calibration of the MS sensor was performed using a suitable reference calibration panel, CRP2 (Figure 3B). Following these procedures, the aerial photogrammetry process commenced (Figure 3C). To account for potential variations in atmospheric conditions, the radiometric calibration of the MS sensor was repeated after each mission.

2.3.2. UAV LiDAR Survey

The subsequent UAV survey mission involved the utilization of the DJI Matrice M300 RTK and the DJI Zenmuse L1 LiDAR payload (Table 2). This particular model of UAV is commonly employed by numerous authors in various studies that necessitate spatial data acquisition with exceptionally high positional accuracy [68–70]. The used laser scanner, DJI Zenmuse L1, incorporates a stabilized three-axis gimbal, an RGB sensor, and an IMU unit. This combination enables the production of a true-color point cloud, using the RGB sensor. The LiDAR Livox sensor within the DJI Zenmuse L1 has an average detection distance of 450 m with 80% reflectivity and 190 m with 10% reflectivity. It can achieve an effective point rate of approximately 240,000 pts/s on a single return, and twice that on multiple returns. Moreover, it can cover an area of approximately 2 km^2 in a single flight [71].

Table 2. DJI Zenmuse L1 LiDAR specifications [71].

Sensor type	LiDAR
System Accuracy (RMS 1σ)	Horizontal: 10 cm from 50 m Vertical: 5 cm from 50 m
Ranging Accuracy (RMS 1σ)[2]	3 cm from 100 m
Yaw Accuracy (RMS 1σ)	Real-time: 0.3°, post-processing: 0.15°
Pitch/Roll Accuracy (RMS 1σ)	Real-time: 0.05°, post-processing: 0.025°

The mission was scheduled to have a duration of one hour and eight minutes. With a ground-sampling distance of 2.73 cm/pix, the point-cloud density for this mission was configured to be 141 points/m^2. The flight altitude for the survey mission was set at 100 m, with a flight speed of 10 m per second. The side overlap for the LiDAR sensor was set to 20%, while for the visible (RGB) sensor, it was set to 37%. The forward overlap for the RGB sensor was set at 70%. Furthermore, the data collection process employed the direct georeferencing method. Before the flight, calibration of the devices was performed to ensure accurate data acquisition and measurements (Figure 4A,B).

Figure 4. (**A**) DJI Matrice M300 RTK pre-flight procedure; (**B**) DJI Zenmuse L1 LiDAR field survey.

2.4. Data Processing

2.4.1. UAV$_{MS}$ Data Processing

The images obtained from the UAV$_{MS}$ mission were primarily geocoded using the UAV's Flylog records and data from the base station. Subsequently, these images were processed using Agisoft Metashape 1.5.11. This software is widely utilized, due to its implementation of structure-from-motion (SfM) and 3D modeling algorithms that rely on the overlap of 2D images.

Through a series of well-defined settings and steps, including photo orientation, the derivation of a dense point cloud, deep filtering, and optimization of sensor locations, a high-quality 3D model was generated. The resulting model was then exported as UAV$_{MS}$.

2.4.2. LiDAR Data Processing

The point cloud acquired from the Zenmuse L1 was processed using the DJI Terra 3.6.0 software. A total of 19 GB of data was collected. First, a high-density decision-making approach was selected to maximize the utilization of all acquired data and produce output results with the highest level of accuracy. Second, the output coordinate system setting was set to HTRS96/TM. To validate the acquired data, a total of 229 checkpoints (CPs) were collected using the RTK GNSS Trimble R12i. Subsequently, the optimization of point-cloud accuracy was performed, followed by the generation of a 3D point cloud. Initially, the output file was in *.pnts* format, but it was transformed into *.las* format.

Using the Spatix 022.028 software, anthropogenic objects and vegetation were excluded from the data. The data harmonization process involved five steps. The first step involved grouping point clouds based on recorded profiles, referred to as dividing trajectories. The second step, called match passes, aimed to reduce inconsistencies across profiles and enhance the internal correctness of the point cloud. In the third step, points that intersected in overlap areas were removed. The fourth step involved smoothing the points and removing noise. The final step before obtaining the ground model or the digital terrain model (DTM) involved data thinning, which entailed removing inactive points to reduce the total data volume.

2.5. Creation of Very-High-Resolution Models/Criteria

The first step in the process of generating the IEI model was the derivation of VHR models/criteria for the GIS-MCDA.

Taking into account the collected data and the factors that affect the imperviousness and infiltration capacity, a total of six criteria were selected and derived: CN, IS, NDVI, slope, TWI, and aspect. Considering the homogeneity of the pedological base in the research area, the inclusion of pedological criteria in the GIS-MCDA process was deemed unnecessary, but it should be included in larger catchments. Furthermore, it should be noted that geological factors have a significant impact on infiltration processes [72]. However, due to the limited availability of detailed VHR spatial data, comprehensive geological information was not available for this relatively small research area.

2.5.1. CN and IS

CN and IS models were generated from the LULC model. The derivation of the LULC model was performed using a hybrid approach that combined geographic object-based image analysis (GEOBIA) [73] with manual improvement techniques [74]. This approach involved the following steps: (1) UAV_{MS} image segmentation; (2) adding training samples; (3) image classification using support vector machine (SVM) and maximum likelihood classifier (MLC); (4) accuracy assessment; (5) improving LULC quality; and (6) adding CN and IS values to LULC classes.

The first step (1) involved UAV_{MS} image segmentation. This step is crucial in GEOBIA, where adjacent pixels are grouped to create image objects that resemble actual geographic objects in the real world [75,76]. Segmentation, performed using an ArcMap 10.4.1.-based procedure based on the mean shift technique, is essential for generating the LULC model. The segment mean shift tool groups pixels with similar spectral, spatial, and geometrical features to identify distinct characteristics or segments in the images. The characteristics of the image segment are influenced by spectral detail, spatial detail, and minimum segment size [77]. Through an iterative process (n = 25), the parameter values were tested to find the optimal combination. The selection of the optimal parameter values was based on a visual assessment of the UAV_{MS} segmented model. The input datasets and parameters pertinent to the segmentation process are delineated in Table 3.

Table 3. Input datasets and parameters of the segmentation process.

Input Raster	UAV_{MS}
Spatial resolution	0.079 m
Source	MicaSense RedEdge-MX Dual MS
Date of acquisition	10 August 2022
Spectral detail	19
Spatial detail	15
Minimum segment size in pixels	20
Band indices	10, 5, 3

In the second step (2), training samples were added. It is often observed that an increased number of high-quality training samples leads to improved overall accuracy when training the classification model [78]. Ye et al. [79] recommended a minimum of 50 samples per class. The sample locations were generated using a probabilistic method of systematic sampling. The select segment tool within the training sample manager in ArcMap 10.4.1. was utilized to add the samples (Figure 5). During the addition process, the optimal number of classes representing the study object, as well as the number of other classes within the observed area, was carefully considered and optimized.

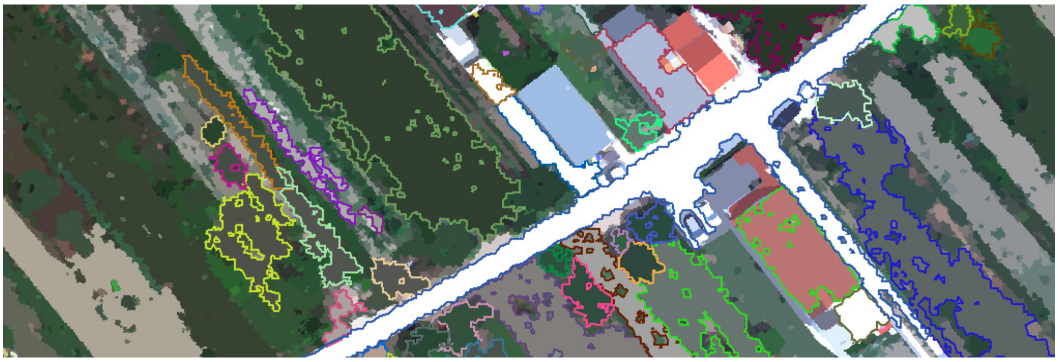

Figure 5. Adding training samples for the LULC model.

In the third step (3), the classification of the segmented UAV_{MS} was carried out using SVM and MLC algorithms. Both of these classification algorithms are integrated within ArcMap 10.4.1. and have been widely utilized by numerous authors [80–83] for the extraction of LULC information. The input parameters utilized for SVM and MLC classifications encompass distinct segment attributes. The color attribute characterizes the average chromaticity color of each segment, providing insight into its color composition. Meanwhile, the mean attribute represents the average digital number (DN) derived from the pixel image, thereby conveying information about the segment's brightness level. Additionally, the STD attribute corresponds to the standard deviation of pixel values within the segment, furnishing details about the variability of pixel intensities. The count attribute signifies the count of pixels composing the segment, reflecting its spatial extent within the image. Moreover, the attributes of compactness and rectangularity quantify geometric properties of the segments. Compactness delineates the circularity or compactness of the segment, with values ranging from 0 to 1, where 1 indicates a perfect circle. Conversely, rectangularity gauges the extent to which the segment approximates a rectangle, with values also ranging from 0 to 1, where 1 indicates a perfect rectangle. These attributes are computed on a per-segment basis and serve as crucial features for the classification algorithms [84]. Employing these attributes as input parameters enables SVM and MLC classifications to discriminate and categorize segments with enhanced precision and accuracy. Furthermore, the generated DTM was incorporated as an additional input raster. Tables 4 and 5 present comprehensive expositions of the input datasets and parameters pertaining to the SVM and MLC classification processes.

Table 4. Input datasets and parameters of the SVM classification process.

Input Raster	Segmented UAV_{MS}
Spatial resolution	0.079 m
Source	MicaSense RedEdge-MX Dual MS
Date of acquisition	10 August 2022
Additional input raster	DTM
Spatial resolution	0.5 m
Source	DJI Zenmuse L1 LiDAR
Date of acquisition	11 August 2022
Max number of samples per class	500
Segment attributes	Color; mean; STD; count; compactness; rectangularity

Table 5. Input datasets and parameters of the MLC classification process.

Input Raster	Segmented UAV_{MS}
Spatial resolution	0.079 m
Source	MicaSense RedEdge-MX Dual MS
Date of acquisition	10 August 2022
Additional input raster	DTM
Spatial resolution	0.5 m
Source	DJI Zenmuse L1 LiDAR
Date of acquisition	11 August 2022
Segment attributes	Color; mean; STD; count; compactness; rectangularity

The fourth step (4) of the GEOBIA process involved determining the most accurate classification algorithm. Accuracy assessment was conducted using overall accuracy (OA), and the kappa coefficient (KC). OA is the ratio of the total number of accurately classified pixels to the total number of pixels in the error matrix [85,86]. The KC measures the correlation between the classified data and the reference data, utilizing the major diagonal of the confusion matrix, as well as the sums of the matrix's columns and rows [87,88].

$$\mathrm{OA} = \sum_{i=1}^{m} Pii \tag{1}$$

$$KC = \frac{N\sum_{i=1}^{r} Pii - \sum_{i=1}^{r}(p_{i+} \times p_{+i})}{N^2 - \sum_{i=1}^{r}(p_{i+} \times p_{+i})} \tag{2}$$

where p_{ii} is the major diagonal element for class I, p_{i+1} is the total number of observations in column i (bottom margin), p_{i+} is the total number of observations in row i (right margin), and m is the number of rows, columns in the error matrix. OA values can range from 0 to 1, with higher values indicating greater accuracy. To assess accuracy, layers of consistently distributed points were generated for the 19 classes in the study area, using the Create Accuracy Assessment Points tool within ArcMap 10.4.1 and a stratified random sampling strategy. These points were strategically placed within the classes, resulting in 1568 point samples. This sampling strategy ensured highly accurate outcomes [89,90]. Each point was assigned a land-cover-type attribute taken from the official vector layer, with cadastral information provided by the city.

In the fifth step (5), the quality of the created LULC was improved. When utilizing very-high-resolution geospatial technologies in urban environments and classifying numerous classes, misclassification becomes a significant concern [91–93]. The selection of appropriate remotely sensed datasets and a suitable classification algorithm are the two key factors for achieving an accurate LULC model [94]. However, the complexity of heterogeneous areas poses a considerable challenge for machine-learning algorithms [95]. Consequently, in regions of the study area where classification accuracy was not satisfactory, manual interventions were employed to enhance the accuracy of the LULC model [51,52,96]. This approach, which combines machine-learning classification algorithms with manual interventions, is commonly referred to as a hybrid approach [97–99]. Manual improvements of selected classes were performed using geometrically referenced data, such as the digital orthophoto (DOP) with a spatial resolution of 3 cm. Additionally, cadastral information was integrated with the DOP, contributing to more precise corrections of misclassified classes.

The final step (6) was adding CN and IS values to LULC classes. The infiltration capacity was described by the CN number, according to the NRCS methodology [37], and corresponding values were added to each LULC class. According to the Croatian pedological map [100] and previous investigations [63,64] the soil in this area can be characterized as alluvial (fluvisol), with good drainage capacity. Therefore, it has been assigned to the hydrological soil group B. Table 6 shows the selected values of the CN for all 19 LULC classes of the hydrological soil group B in the study area. All CN values were selected from the relevant literature [37,38]. Higher CN numbers corresponded to a lower infiltration capacity, and vice versa. The IS model was a Boolean mask, where false value (0) denotes impervious LULC classes, such as asphalt, buildings, greenhouses, and water, while true (1) denotes pervious LULC classes, such as orchard, vineyard, olive grove, low vegetated, and high vegetation.

Table 6. LULC classes and corresponding CN and IS values for the hydrological soil group B [37,38].

LULC	CN	IS	LULC	CN	IS	LULC	CN	IS
Agricultural road	80	1	High vegetation	62	1	Orchard	52	1
Arable land	69	1	Junk yard	69	1	Railway	80	1
Asphalt	98	0	Lawn	69	1	Reed	81	1
Buildings	90	0	Low vegetation	65	1	Tangerines	52	1
Embankment	80	1	Macadam	80	1	Vineyard	52	1
Greenhouse	90	0	Olive grove	52	1	Water	100	0
Homestead	85	1						

2.5.2. Normalized Difference Vegetation Index (NDVI)

One of the most commonly used vegetation indices in remote sensing is the normalized difference vegetation index (NDVI) [101–103]. Many authors have chosen the NDVI as a parameter for modeling impervious surfaces [104–108]. The NDVI has a significant role in impervious-surface modeling, as it quantifies the difference between the infrared component of the electromagnetic spectrum, which is highly reflected by vegetation, and the visible portion of the red spectrum, which is extensively absorbed by vegetation [109].

$$NDVI = \frac{NIR - R}{NIR + R} \quad (3)$$

The multispectral bands from the sensor were combined to generate the NDVI, which can be derived using various tools in ArcMap 10.4.1. One of these tools is the Raster Calculator, which allows the creation and execution of different commands and variables to convert existing raster layers into new raster models that represent vegetation indices. Through the tool's dialogue box, users can select appropriate options and incorporate numerical values and mathematical operators to construct the required equations. Table 7 displays the input datasets and parameters used in the process of generating the NDVI.

Table 7. Input datasets and parameters employed in the generation of the NDVI criterion.

Input Raster	UAV_{MS}
Spatial resolution	0.079 m
Source	MicaSense RedEdge-MX Dual MS
Date of acquisition	10 August 2022
Spectral bands	NIR, R

2.5.3. Slope

The significance of slope, as a crucial factor for infiltration modeling [110] and imperviousness modeling [111,112], is emphasized in numerous studies. The variations in infiltration within the same land-cover class, but with different slope angles, highlight the influence of slope on the infiltration process [5,35,113]. Slope angle directly affects infiltration, runoff frequency, and velocity. Flat terrain is more susceptible to flooding, as runoff is slower and larger amounts of water accumulate after precipitation events, while steep terrain experiences less risk of flooding, due to higher runoff velocity [35,114]. To calculate the slope angles, the created DTM was processed using the spatial analyst tool in ArcMap 10.4.1. Table 8 exhibits the input datasets and parameters employed in the generation of the slope criterion. The established value of the Z factor, which is utilized to adjust measurement units in cases of non-alignment, was set to 1, as the x, y, and z values are all expressed in meters.

Table 8. Input datasets and parameters employed in the generation of the slope criterion.

Input Raster	DTM
Spatial resolution	0.5 m
Source	DJI Zenmuse L1 LiDAR
Date of acquisition	11 August 2022
Output measurement	Degree
Z factor	1

2.5.4. Topographic Wetness Index (TWI)

The topographic wetness index (TWI) is a hydrological metric used to assess the potential wetness of a specific terrain, indicating its propensity to retain water [115,116]. By utilizing the TWI, it becomes possible to identify and analyze various waterlogged regions, such as swamps, sinkholes, ravines, and river valleys, which exhibit high values of this index. Conversely, drier areas, such as steep slopes and higher elevations, exhibit low values of the TWI. In this research, the TWI was computed using the topographic wetness index tool available in the Saga GIS 7.8.2. extension for ArcMap 10.4.1. The calculation of the TWI required input data, such as slope and catchment area size. The input datasets and the parameters employed in the generation of the TWI criterion are shown in Table 9. In the process of generating the TWI, the standard method was employed, and conversion was not selected, as the area was already specified as a specific catchment area.

Table 9. Input datasets and parameters employed in the generation of the TWI criterion.

Input Raster	Slope
Spatial resolution	0.5 m
Source	DJI Zenmuse L1 LiDAR
Date of acquisition	11 August 2022
Catchment area	Study area raster layer
Spatial resolution	0.5 m
Source	MicaSense RedEdge-MX Dual MS
Date of acquisition	10 August 2022
Area conversion	No conversion
Method	Standard

2.5.5. Slope Orientation (Aspect)

The aspect also has a role in modeling infiltration. Some studies [117,118] established a correlation between infiltration capacity and daily temperature variations, which are higher on south-oriented slopes. This implies that on slopes oriented toward the north, the soil tends to be wetter, resulting in lower permeability.

To create the slope-orientation model, the aspect tool was utilized. This tool, available within ArcMap 10.4.1., visualizes the direction of the steepest value change from each cell to its neighboring cells. The measurement is presented in degrees, clockwise, completing a full circle from 0 degrees (representing north) to 360 degrees (again, representing a northward direction). The input datasets and the parameters of the slope-orientation extraction process are shown in Table 10.

Table 10. Input datasets and parameters of the slope orientation extraction process.

Input Raster	Slope
Spatial resolution	0.5 m
Source	DJI Zenmuse L1 LiDAR
Date of acquisition	11 August 2022

2.6. GIS-MCDA

Multicriteria GIS decision analysis (GIS-MCDA) allows decision-makers to incorporate geographical information and spatial relationships into the decision-making process. It enables the evaluation and comparison of multiple criteria associated with different locations or spatial units [119]. This approach is particularly useful in situations where decision-making involves selecting a location or prioritizing actions in a geographic context.

The methodological framework of the GIS-MCDA consists of three main steps: value scaling (or standardization), criterion weighting, and aggregation of standard criteria and weight coefficients (W_i) [119].

In the first step (1), created criteria were standardized. The process of standardization was performed using the fuzzy logic approach in ArcMap 10.4.1. software. The fuzzy membership tool was utilized to standardize the raster criteria, based on a chosen fuzzification algorithm. The standardization was performed on a scale ranging from 0 to 1, where a value of 1 indicated maximum membership strength, gradually decreasing toward 0. The linear method was specifically employed, assigning higher values to impervious classes [120]. LULC classes with CN values greater than 0.9 (asphalt, buildings, greenhouses, and water) were extracted as a Boolean criterion (IS model) that is not affected by other used criteria, considering that they are impervious and/or related to very low infiltration. The second step (2) involved the utilization of the analytic hierarchy process (AHP) to calculate the required W_i (Table 11). Numerous methods for calculating weight coefficients (CWC) are available, such as the best–worst method (BWM), the simple multi-attribute rating technique (SMART), the full-consistency method (FUCOM), the swing method, the trade-off method, the point-allocation method, the direct-rating method, and the AHP [121,122]. Each of the existing CWC methods comes with its own set of advantages and disadvantages, depending on the research goals and objectives [121]. Among these methods, the AHP is commonly utilized [123–126]

Table 11. The AHP preference matrix and assigned W_i for the five created criteria.

	CN	**NDVI**	**SLOPE**	**TWI**	**ASPECT**	W_i
CN	1	3	4	6	8	**50.37**
NDVI	0.333	1	2	4	6	**24.26**
SLOPE	0.25	0.5	1	2	4	**13.8**
TWI	0.167	0.25	0.5	1	2	**7.31**
ASPECT	0.125	0.167	0.25	0.5	1	**4.27**

The LULC criterion was reclassified, based on the CN values of each class, and was considered the most crucial factor in infiltration mapping, receiving the highest assigned W_i. The NDVI criterion held the next level of importance, as it effectively distinguished between permeable and impervious surfaces. Furthermore, the criteria of slope and the TWI were assigned relatively lower W_i, while the aspect received the lowest W_i, due to the lowest influence on infiltration.

The determination of W_i in the AHP involved an iterative process (n = 25), wherein various preference strengths were tested between criteria. Careful attention wa given to ensured that the resulting consistency ratio (CR) did not exceed the threshold of 0.1 [127]. During each iteration, preference judgments were reevaluated, adjusting the preference strengths within the matrix. The W_i was then recalculated, based on these revised judgments. This iterative cycle continued until a satisfactory level of CR was achieved, ensuring that the preference judgments aligned more accurately with the decision-makers' intentions.

In the final step, the GIS-MCDA model of IEI was created, based on the aggregation of standardized criteria and their W_i.

3. Results and Discussion

3.1. Acquired VHR Data

A total of 34,330 MS images were acquired. Considering that the MicaSense RedEdge-MX Dual Camera sensor captures the area simultaneously with 10 independent spectral bands at each location, the photos were gathered from 3433 different locations.

The LiDAR survey resulted in the acquisition of 19 GB of data. Each file contained a specific type of information that was essential in data processing. For example, the *.imu* file recorded the original x, y, and z displacement data during the survey, while the *.rtk* file recorded the status of the main GNSS and its characteristics. The photos were in *.jpg* format and were primarily used to colorize the dense point clouds.

3.2. Derived VHR Models

3.2.1. UAVMS

The MS model, with a spatial resolution of 7.98 cm, consisted of 10 different spectral bands (Figure 6A,B). These bands were modified individually to achieve the optimal spectral band arrangement for the observed area. The accuracy of the MS was assessed, based on the nine collected CPs, yielding a root mean square error (RMSE) of 0.0336 m. This indicated a high level of accuracy and agreement between the observed data and the reference data. The MS model was utilized to create the VHR LULC and NDVI models.

Figure 6. The MS model: (**A**) RGB (6-4-2); (**B**) false color (10-7-5).

3.2.2. DSM and DTM

After processing LiDAR data in DJI Terra, a digital surface model (DSM) was generated (Figure 7A). Subsequently, a very-high-resolution (VHR) DTM was created (Figure 7B), using Spatix software. The accuracy of the LiDAR model was evaluated using 229 CPs, resulting in an RMSE value of 0.0387 m. This indicated a high level of accuracy and agreement between the LiDAR-derived model and the reference data. Despite the potential for a higher spatial resolution in the DTM, the processing complexity necessitated exporting the model at a spatial resolution of 0.5 m. The resulting model was utilized to derive various criteria, including the slope, the TWI, and the aspect.

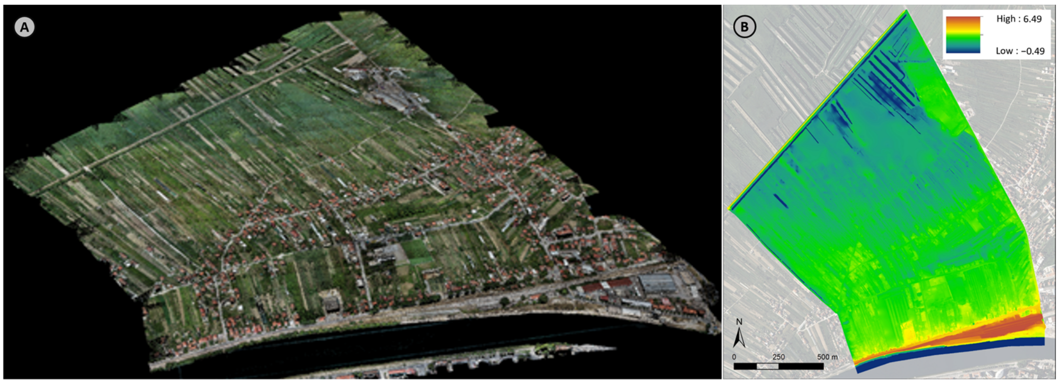

Figure 7. (**A**) The DSM; (**B**) the DTM.

3.2.3. LULC, CN, and IS

By visually interpreting the generated models, a model with a spectral detail value of 19, a spatial detail value of 15, and a minimum segment size of 20 was selected (Figure 8A). These values were consistent with those used in previous research employing the GEOBIA approach [90,128–130]. A total of 6489 samples was added across 19 classes on the segmented model to generate an SVM model (Figure 8B) and an MLC (Figure 8C) model.

Figure 8. (**A**) The segmented 20-19-15 model; (**B**) the SVM model; (**C**) the MLC model.

Among the two classification algorithms used in the GEOBIA process, the SVM algorithm demonstrated higher accuracy, with an OA measure of 0.6687 and a KC accuracy measure of 0.3512, while the MLC algorithm resulted in an OA measure of 0.6152 and a KC accuracy measure of 0.2926 (Table 12). The calculated low-accuracy values can be attributed to the presence of a significant number of classes that exhibited similar spectral values [131–133]. This similarity posed challenges in accurately distinguishing and classifying these classes, resulting in reduced accuracy measures. The overlapping spectral characteristics made it difficult for the classification algorithms to accurately assign pixels to their respective classes, leading to misclassifications and reduced overall accuracy.

Table 12. GEOBIA accuracy assessment measures results.

	OA	KC
SVM	0.6687	0.3512
MLC	0.6152	0.2926

The SVM classification model was generated using a cell size of 0.079 m, and it employed an unsigned integer (8-bit) pixel type and depth. With pyramids set at level 7 and a resampling technique of nearest neighbor, the model achieved better accuracy than that of the MLC model, by effectively discerning spatial patterns and spectral characteristics within the segmented UAV_{MS} data. The chosen parameters ensured optimal OA in classifying LULC.

VHR data, like the data collected for this research (<8 cm), posed a challenge due to their high level of detail, which made classification intricate when creating an LULC model. In essence, there was a multitude of potential classes, such as the diverse types of roof tiles, some of which may be covered in moss and other debris. In addition, there were other intricate details captured by the VHR multispectral camera, including vehicles on roads. Due to these complexities, it was logical to expect that classification algorithms may not have achieved a high level of accuracy. Therefore, manual corrections were often employed, allowing for interventions in areas with significant errors, thereby enhancing the quality of the LULC model [51,52]. After the manual intervention, the classified SVM model was significantly improved (KC = 0.9524), particularly in regions of the study area where the accuracy was not satisfactory. The generated LULC model (Figure 9) exhibited a high level of accuracy in distinguishing impervious surfaces within the study area. Among the various LULC classes, the most dominant were low-vegetation areas, covering 47.54 hectares, and arable-land areas, covering 25.42 hectares. The impervious classes, including asphalt, buildings, greenhouses, and water, collectively covered 24.41 hectares within the study area. Those classes were singled out as a special (Boolean) criterion (IS model), as their permeability was not influenced by any other created criteria. In the final step, attributes related to infiltration capacity were added to different classes, resulting in the generation of a very-high-quality CN model. To ensure the harmonization of input data for subsequent analyses, the spatial resolution of the generated model was reduced to 0.5 m.

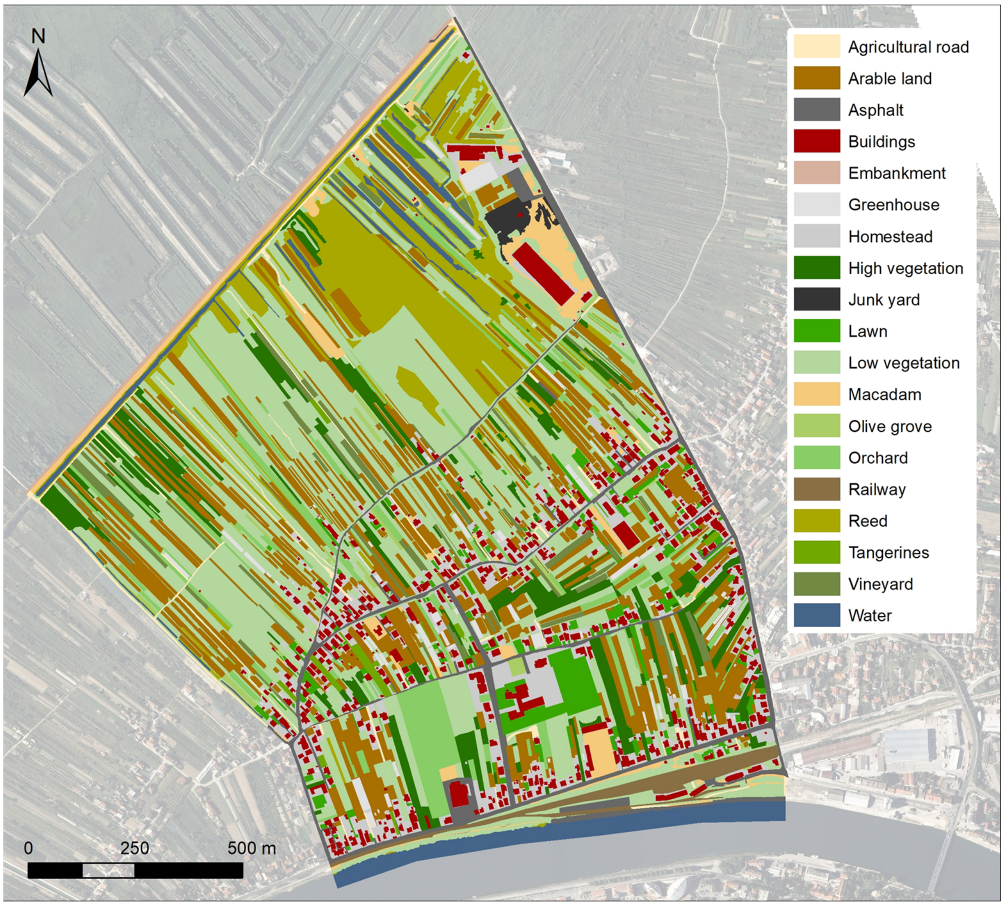

Figure 9. The LULC model.

3.2.4. The NDVI

After applying the Raster Calculator tool, the NDVI model for the research area was generated (Figure 10A). The NDVI model exhibited a range of values from −1 to 1, where higher values indicated the presence of healthy vegetation and lower values indicated the presence of unhealthy vegetation. As impervious surfaces lack vegetation, they exhibit low NDVI values, enabling the differentiation of impervious areas from vegetated areas. This makes NDVI a valuable criterion for identifying and mapping impervious surfaces [104–108]. In the northern part of the research area, the index values were notably high, primarily due to the presence of irrigated and fertile soil encompassing orchards, tangerine groves, olive groves, vineyards, and other types of high and low vegetation. Additionally, this region is characterized by the occurrence of reeds, which are indicative of the swampy nature of the area. Lower values were observed in the southern and eastern regions of the study area, and were primarily attributed to the presence of anthropogenic structures and objects. The spatial resolution of the NDVI model was also reduced to 0.5 m to align with the data for GIS-MCDA.

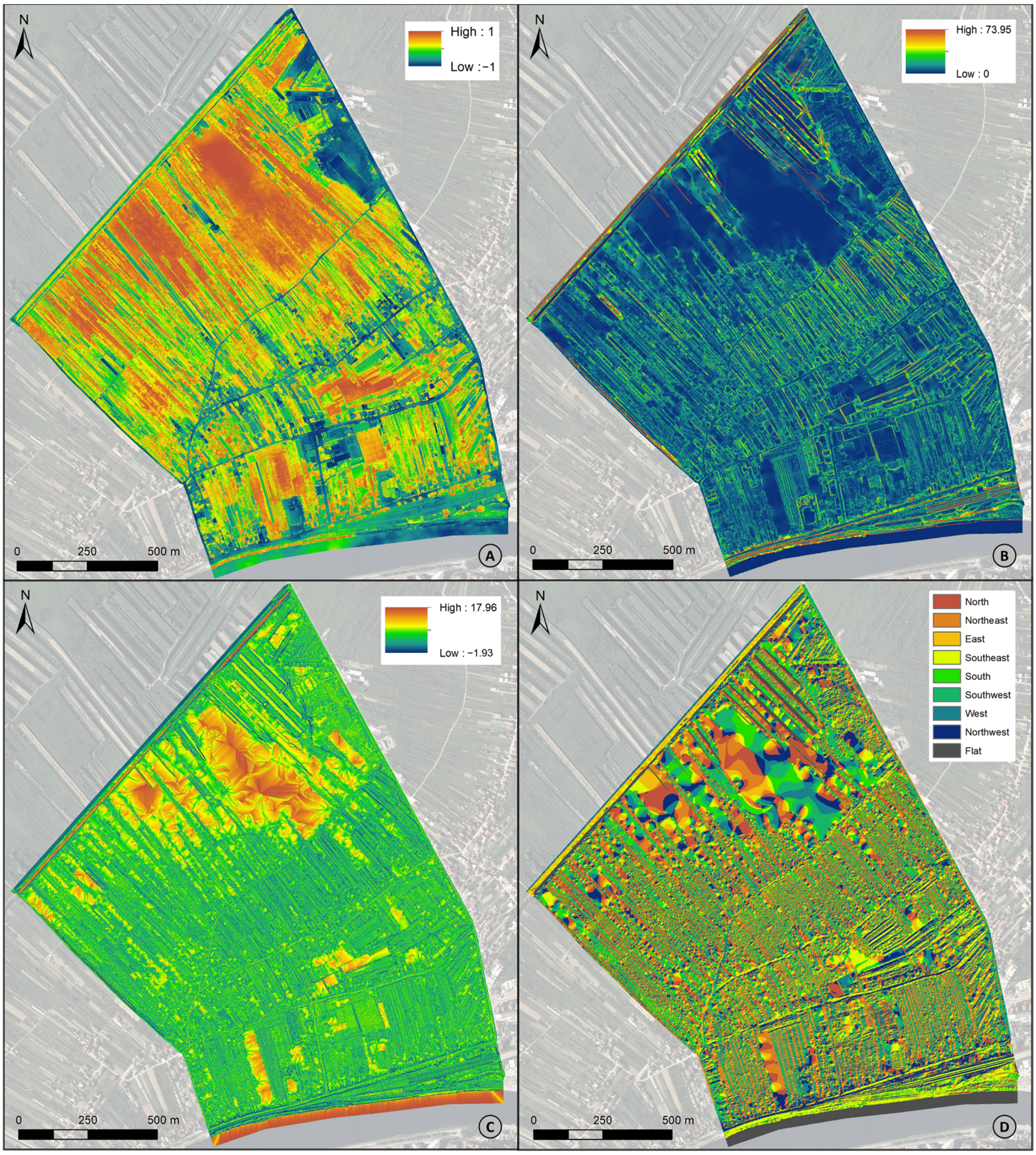

Figure 10. (**A**) The NDVI model; (**B**) the slope model; (**C**) the TWI model; (**D**) the aspect model.

3.2.5. Slope

The research area exhibits predominantly flat terrain with minor slopes (Figure 10B). However, notable slopes were observed in specific regions, such as embankments, water channels, and populated areas that were elevated above the surrounding terrain by filling materials. Sugianto et al. [114] indicated that the highest susceptibility to flooding occurs in areas with a slope ranging from 0% to 5.5%, due to the accumulation of runoff water. Conversely, steeper areas, with slopes exceeding 30%, have lower flood risk, as surface runoff in such slopes tends to be much faster.

3.2.6. The TWI

The TWI criterion serves as a useful indicator for discerning areas that are prone to water accumulation within the topographic basin. Regions exhibiting a lower propensity for water accumulation also display reduced water infiltration. Within the research area, the

TWI values were influenced by the relief's morphological characteristics. Elevated sections, such as the embankment located along the northern part of the study area, exhibited lower TWI values, signifying minimal or negligible water accumulation (Figure 10C). Conversely, lower-lying portions of the relief demonstrated higher TWI values, indicating a greater potential for significant water accumulation. Based on the TWI analysis, two distinct areas of water accumulation were identified within the study area. The first area encompasses the swampy region and water channels, while the second area corresponds to the Neretva River.

3.2.7. Aspect Model

The created aspect model represented the slope orientation in the study area (Figure 10D). Braga et al. [118] emphasized the significance of soil temperature as a key factor influencing hydraulic conductivity and, consequently, the infiltration rate. They highlighted that temperature plays a crucial role, with higher temperatures during warmer periods impacting the infiltration rate by up to 56%. It is postulated that in the case of more northerly oriented slopes, the colder temperatures contributed to increased soil moisture, thereby influencing reduced permeability.

3.3. GIS-MCDA

After generating the criteria models, the fuzzy membership tool and the linear membership method were employed to scale the values from 0 to 1, where higher values represented a higher IEI. The 19 classes extracted from the LULC model were reclassified based on the CN value, thereby forming the CN criterion. The values were rescaled from the original 0–100 scale to the 0–1 scale, where higher values indicated higher infiltration efficiency, receiving the maximum membership value (Figure 11A). Similarly, the NDVI values were transformed to the 0–1 scale, where lower values represented increased imperviousness and, therefore, lower infiltration efficiency (Figure 11B). The slope criterion was standardized, such that a higher degree of slope corresponded to low infiltration efficiency (Figure 11C). The TWI criterion was also standardized, with lower values indicating lower infiltration efficiency, where a value of 0 corresponded to impervious surfaces (Figure 11D). The aspect criterion was standardized, with values closer to the north signifying lower infiltration efficiency, while more southerly oriented slopes indicated higher infiltration efficiency (Figure 11E). Finally, a Boolean mask (IS model) was applied, representing fully impervious surfaces, such as asphalt, buildings, greenhouses, and water (Figure 11F). After conducting 25 iterations of the AHP and selecting the final values for W_i, the CR was calculated to be 0.02. This value fell within the acceptable range (<0.1), indicating satisfactory consistency in the decision-making process [127]. This approach aligned with a previous study [134], which employed a similar method on 0.5 m data, resulting in significant improvements in the input spatial data for VHR hydrologic-hydraulic modeling in urban areas.

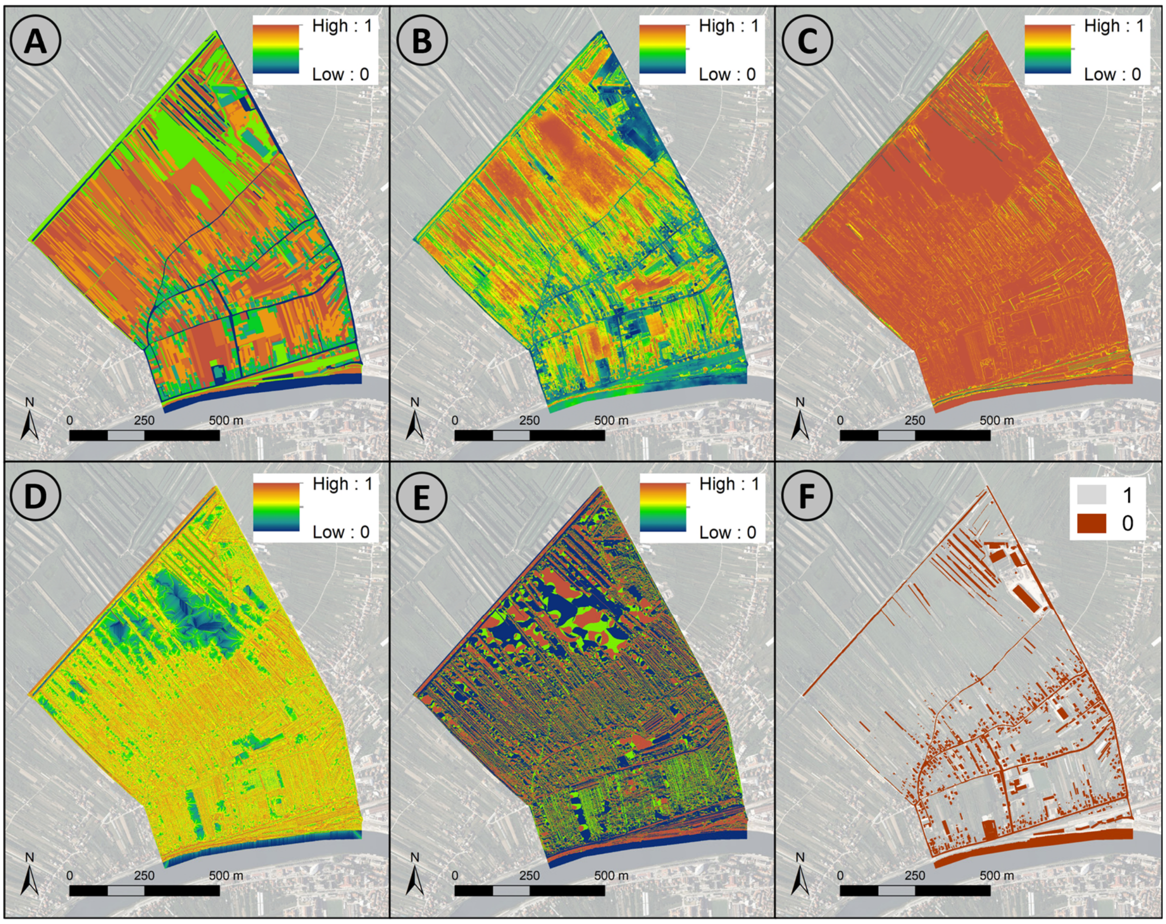

Figure 11. Standardized criteria for the GIS-MCDA: (**A**) CN; (**B**) NDVI; (**C**) slope; (**D**) TWI; (**E**) aspect; (**F**) IS model (Boolean).

Infiltration Efficiency Index Model

By aggregating standardized criteria with specific Wi, the final VHR IEI model (0.5 m), with values ranging from 0 to 0.71, was generated (Figure 12). The model revealed that 14.89% of the research area is covered by very low IEI values (0–0.1), which are related to impervious surfaces. This percentage signified a favorable condition, in comparison to urban areas worldwide [135–137]. However, it is important to highlight that the city of Metković encompasses extensive agricultural regions that significantly impacted this result. The majority of the research area (62.79%) exhibits a higher IEI, with values above 0.5. These areas are predominantly characterized by agricultural land use, encompassing orchards, tangerines, olive groves, vineyards, and a diverse range of low-lying and high vegetation on flat terrain. The research area exhibited a maximum IEI value of 0.71.

Urban land can have a significant impact on flooding, often increasing the risk and severity of floods, due to changes in land cover, drainage systems, and impermeable surfaces that can lead to increased runoff during heavy rainfall events [138]. In this IEI model, urban land was not utilized as one of the input criteria. This decision was made because the impermeability of urban surfaces was already incorporated as one of the input criteria, in the form of the IS model (Boolean). The morphological spatial patterns of urban land influence meso-level research. However, at the micro-level, which is the focus of this model, it did not have a significant impact.

Nevertheless, the urban-land criterion can be added as one of the input criteria, together with the IEI model, when developing susceptibility models using GIS-MCDA methodology. Additionally, the incorporation of a thermal camera can provide significant assistance in the mapping of ISs and infiltration efficiency [139–141]. However, caution should be exercised in interpreting these data, as the presence of tall buildings and trees can create shaded areas with considerably lower temperatures, making it challenging to establish an optimal threshold [142,143]. Previous studies predominantly focused on lower-spatial-resolutions satellite data [5,9,17–27,32,135–137,139]. In contrast, this approach offered notable advantages by using advanced GST, which facilitated the generation of VHR models and enabled the mapping of infiltration efficiency at a micro level of research. This model provided input spatial data for GIS hydrological analyses in this research area and will be employed as an integral component of a project aimed at the creation of hazard and risk maps for pluvial and fluvial floods. Furthermore, the precise identification of the IEI is crucial in predicting land-surface temperature and studying urban heat islands [144], so the methodology presented in this study can also be effectively employed for those purposes.

Figure 12. IEI model of the study area.

4. Conclusions

The utilization of advanced GST, including MS sensors and LiDAR, facilitated the acquisition of spatial data at VHR. These high-quality data enabled the derivation of precise and accurate models. By incorporating these models into the GIS-MCDA process, highly accurate outcomes were obtained, considering the spatial resolution and accuracy of input data and derived models. Numerous authors have actively engaged in the field of flood susceptibility modeling. However, it is worth noting that, to date, there has been a notable absence of investigations that incorporated the spatial parameter of infiltration as an input criterion. The current scientific study fills this gap by introducing an innovative approach for mapping the IEI at VHR through the application of GIS-MCDA. This methodology not only expands the horizons of flood-susceptibility assessment, but also underscores the importance of considering infiltration in such models, shedding new light on flood-risk management and urban planning.

The study developed a VHR IEI model from six specific criteria that produced values ranging from 0 to 0.71. The model's findings indicated that around 14.89% of the studied area has a very low IEI, primarily due to ISs. This percentage is relatively favorable, when compared to urban areas globally. However, it is important to note that the presence of extensive agricultural regions in the city of Metković had a significant impact on this result. The majority acreage of the research area, accounting for 62.79%, exhibited higher IEI values, exceeding 0.5. These areas are characterized by agricultural land use, including orchards, tangerines, olive groves, vineyards, and various types of vegetation on flat terrain. The highest observed IEI value within the research area was 0.71. This suggested that the region's land-use composition plays a crucial role in influencing infiltration-efficiency patterns.

One of the limitations of this work was related to the uncertainty of the MCDA and the choice of W_i for the input criteria, as well as the lack of validation. In future research, the focus will be directed toward examining the influence of each utilized criterion and validating the accuracy of the proposed IEI model. The impact of different criteria can be assessed by measuring infiltration in various scenarios, combining the effects of different criteria at locations determined through GIS-MCDA. Field measurements at these locations can then provide the validation of the final model. The main purpose of this work was to introduce a new concept of the IEI, which encompassed all influencing parameters, such as LULC (indirectly), CN, ISs, slope, vegetation health, wetness, and temperature, into a single index that is more suitable for spatial GIS analyses than conventional infiltration models.

The IEI model developed for the research area in Metković showcased excellent differentiation between permeable and impervious surfaces, as evidenced by the high accuracy achieved in the improved final LULC model. The application of GIS-MCDA allowed the examination of variations in surface infiltration throughout the study area. The generated IEI model holds great significance as an input spatial criterion for GIS hydrological analyses in the study area. The IEI has practical value for various stakeholders, including experts, decision-makers, and those interested in the research topic. For urban planners and engineers, the IEI can inform sustainable urban development by highlighting areas where water infiltration is optimal, aiding in the design of effective drainage systems and reducing the risk of urban flooding. Environmental agencies and policymakers can use the IEI to assess the impact of land-use changes on local hydrology and to plan mitigation strategies for flood-risk reduction. Furthermore, the IEI can guide researchers in identifying areas that are prone to flooding, allowing for targeted studies and resource allocation. Ultimately, the index serves as a valuable tool for informed decision-making and sustainable land-management practices.

Author Contributions: Conceptualization, A.Š., L.P., N.K. and M.J.; methodology, A.Š., L.P., R.M. and N.K.; software, A.Š., F.D. and D.R.; validation, N.K., F.D., M.J. and D.R.; formal analysis, F.D. and D.R.; investigation, L.P., R.M. and N.K.; resources, A.Š.; data curation, A.Š., L.P. and R.M.; writing—original draft preparation, A.Š., L.P. and R.M.; writing—review and editing, N.K., F.D., M.J. and D.R.; visualization, L.P., R.M. and F.D.; supervision, A.Š., N.K. and M.J.; project administration, L.P. and R.M.; funding acquisition, A.Š. All authors have read and agreed to the published version of the manuscript.

Funding: This research was carried out within the Interreg Strategic Development of Flood Management (STREAM) project, funded by the Italy–Croatia cross-border cooperation program 2014–2020, and by project UIP-2017-05-2694, which is financially supported by the Croatian Science Foundation. The acquired skills, knowledge, and results from this research were used to meet the needs of the STREAM project.

Data Availability Statement: The data presented in this study are available on request from the corresponding author.

Conflicts of Interest: The authors declare no conflict of interest.

References

1. Arnold, C.L.; Gibbons, C.J. Impervious Surface Coverage: The Emergence of a Key Environmental Indicator. *J. Am. Plan. Assoc.* **1996**, *62*, 243–258. [CrossRef]
2. Weng, Q. Remote Sensing of Impervious Surfaces in the Urban Areas: Requirements, Methods, and Trends. *Remote Sens. Environ.* **2012**, *117*, 34–49. [CrossRef]
3. Hallegatte, S.; Green, C.; Nicholls, R.J.; Corfee-Morlot, J. Future Flood Losses in Major Coastal Cities. *Nat. Clim. Chang.* **2013**, *3*, 802–806. [CrossRef]
4. Duan, C.; Zhang, J.; Chen, Y.; Lang, Q.; Zhang, Y.; Wu, C.; Zhang, Z. Comprehensive Risk Assessment of Urban Waterlogging Disaster Based on MCDA-GIS Integration: The Case Study of Changchun, China. *Remote Sens.* **2022**, *14*, 3101. [CrossRef]
5. Yu, H.; Zhao, Y.; Fu, Y.; Li, L. Spatiotemporal Variance Assessment of Urban Rainstorm Waterlogging Affected by Impervious Surface Expansion: A Case Study of Guangzhou, China. *Sustainability* **2018**, *10*, 3761. [CrossRef]
6. Sohn, W.; Kim, J.-H.; Li, M.-H.; Brown, R.D.; Jaber, F.H. How Does Increasing Impervious Surfaces Affect Urban Flooding in Response to Climate Variability? *Ecol. Indic.* **2020**, *118*, 106774. [CrossRef]
7. Doerr, S.H.; Shakesby, R.A.; Walsh, R.P.D. Soil Water Repellency: Its Causes, Characteristics and Hydro-Geomorphological Significance. *Earth-Sci. Rev.* **2000**, *51*, 33–65. [CrossRef]
8. Brun, S.E.; Band, L.E. Simulating Runoff Behavior in an Urbanizing Watershed. *Comput. Environ. Urban Syst.* **2000**, *24*, 5–22. [CrossRef]
9. Fu, Y.; Liu, K.; Shen, Z.; Deng, J.; Gan, M.; Liu, X.; Lu, D.; Wang, K. Mapping Impervious Surfaces in Town–Rural Transition Belts Using China's GF-2 Imagery and Object-Based Deep CNNs. *Remote Sens.* **2019**, *11*, 280. [CrossRef]
10. Ellis, J.B. Sustainable Surface Water Management and Green Infrastructure in UK Urban Catchment Planning. *J. Environ. Plan. Manag.* **2013**, *56*, 24–41. [CrossRef]
11. Wu, C. Quantifying High-resolution Impervious Surfaces Using Spectral Mixture Analysis. *Int. J. Remote Sens.* **2009**, *30*, 2915–2932. [CrossRef]
12. Shuster, W.D.; Bonta, J.; Thurston, H.; Warnemuende, E.; Smith, D.R. Impacts of Impervious Surface on Watershed Hydrology: A Review. *Urban Water J.* **2005**, *2*, 263–275. [CrossRef]
13. Dietz, M.E.; Clausen, J.C. Stormwater Runoff and Export Changes with Development in a Traditional and Low Impact Subdivision. *J. Environ. Manag.* **2008**, *87*, 560–566. [CrossRef]
14. Liu, Z.; Wang, Y.; Li, Z.; Peng, J. Impervious Surface Impact on Water Quality in the Process of Rapid Urbanization in Shenzhen, China. *Environ. Earth Sci.* **2013**, *68*, 2365–2373. [CrossRef]
15. Kim, H.; Jeong, H.; Jeon, J.; Bae, S. The Impact of Impervious Surface on Water Quality and Its Threshold in Korea. *Water* **2016**, *8*, 111. [CrossRef]
16. Feng, B.; Zhang, Y.; Bourke, R. Urbanization Impacts on Flood Risks Based on Urban Growth Data and Coupled Flood Models. *Nat. Hazards* **2021**, *106*, 613–627. [CrossRef]
17. Deng, C.; Wu, C. BCI: A Biophysical Composition Index for Remote Sensing of Urban Environments. *Remote Sens. Environ.* **2012**, *127*, 247–259. [CrossRef]
18. Liu, C.; Shao, Z.; Chen, M.; Luo, H. MNDISI: A Multi-Source Composition Index for Impervious Surface Area Estimation at the Individual City Scale. *Remote Sens. Lett.* **2013**, *4*, 803–812. [CrossRef]
19. Sun, G.; Chen, X.; Jia, X.; Yao, Y.; Wang, Z. Combinational Build-Up Index (CBI) for Effective Impervious Surface Mapping in Urban Areas. *IEEE J. Sel. Top. Appl. Earth Obs. Remote Sens.* **2016**, *9*, 2081–2092. [CrossRef]
20. Wu, C. Normalized Spectral Mixture Analysis for Monitoring Urban Composition Using ETM+ Imagery. *Remote Sens. Environ.* **2004**, *93*, 480–492. [CrossRef]
21. Herold, M.; Roberts, D.A.; Gardner, M.E.; Dennison, P.E. Spectrometry for Urban Area Remote Sensing—Development and Analysis of a Spectral Library from 350 to 2400 Nm. *Remote Sens. Environ.* **2004**, *91*, 304–319. [CrossRef]
22. Yang, J.; He, Y. Automated Mapping of Impervious Surfaces in Urban and Suburban Areas: Linear Spectral Unmixing of High Spatial Resolution Imagery. *Int. J. Appl. Earth Obs. Geoinf.* **2017**, *54*, 53–64. [CrossRef]
23. Okujeni, A.; van der Linden, S.; Tits, L.; Somers, B.; Hostert, P. Support Vector Regression and Synthetically Mixed Training Data for Quantifying Urban Land Cover. *Remote Sens. Environ.* **2013**, *137*, 184–197. [CrossRef]
24. Ou, J.; Liu, X.; Liu, P.; Liu, X. Evaluation of Luojia 1-01 Nighttime Light Imagery for Impervious Surface Detection: A Comparison with NPP-VIIRS Nighttime Light Data. *Int. J. Appl. Earth Obs. Geoinf.* **2019**, *81*, 1–12. [CrossRef]
25. Sun, Z. Estimating Urban Impervious Surfaces from Landsat-5 TM Imagery Using Multilayer Perceptron Neural Network and Support Vector Machine. *J. Appl. Remote Sens.* **2011**, *5*, 053501. [CrossRef]
26. Okujeni, A.; Canters, F.; Cooper, S.D.; Degerickx, J.; Heiden, U.; Hostert, P.; Priem, F.; Roberts, D.A.; Somers, B.; van der Linden, S. Generalizing Machine Learning Regression Models Using Multi-Site Spectral Libraries for Mapping Vegetation-Impervious-Soil Fractions across Multiple Cities. *Remote Sens. Environ.* **2018**, *216*, 482–496. [CrossRef]

27. Zhang, L.; Zhang, M.; Yao, Y. Mapping Seasonal Impervious Surface Dynamics in Wuhan Urban Agglomeration, China from 2000 to 2016. *Int. J. Appl. Earth Obs. Geoinf.* **2018**, *70*, 51–61. [CrossRef]
28. The European Environment. State and Outlook 2020: Knowledge for Transition to a Sustainable Europe—European Environment Agency. Available online: https://www.eea.europa.eu/soer/2020 (accessed on 5 June 2023).
29. Vysna, V.; Maes, J.; Petersen, J.-E.; La Notte, A.; Vallecillo, S.; Aizpurua, N.; Ivits, E.; Teller, A. *Accounting for Ecosystems and Their Services in the European Union (INCA): Final Report from Phase II of the INCA Project Aiming to Develop a Pilot for an Integrated System of Ecosystem Accounts for the EU: 2021 Edition*; Publications Office of the European Union: Luxembourg, 2020; ISBN 978-92-76-17401-1.
30. Strand, G.-H. Accuracy of the Copernicus High-Resolution Layer Imperviousness Density (HRL IMD) Assessed by Point Sampling within Pixels. *Remote Sens.* **2022**, *14*, 3589. [CrossRef]
31. Krvavica, N.; Šiljeg, A.; Horvat, B.; Panđa, L. Pluvial Flash Flood Hazard and Risk Mapping in Croatia: Case Study in the Gospić Catchment. *Sustainability* **2023**, *15*, 1197. [CrossRef]
32. Imperviousness—Copernicus Land Monitoring Service. Available online: https://land.copernicus.eu/pan-european/high-resolution-layers/imperviousness (accessed on 30 April 2023).
33. Mangala, O.S.; Toppo, P.; Ghoshal, S. Study of Infiltration Capacity of Different Soils. *Int. J. Trend Res. Dev.* **2016**, *3*, 388–390.
34. Horton, R.E. An Approach Toward a Physical Interpretation of Infiltration-Capacity. *Soil Sci. Soc. Am. J.* **1941**, *5*, 399–417. [CrossRef]
35. Yimer, F.; Messing, I.; Ledin, S.; Abdelkadir, A. Effects of Different Land Use Types on Infiltration Capacity in a Catchment in the Highlands of Ethiopia. *Soil Use Manag.* **2008**, *24*, 344–349. [CrossRef]
36. Sun, D.; Yang, H.; Guan, D.; Yang, M.; Wu, J.; Yuan, F.; Jin, C.; Wang, A.; Zhang, Y. The Effects of Land Use Change on Soil Infiltration Capacity in China: A Meta-Analysis. *Sci. Total Environ.* **2018**, *626*, 1394–1401. [CrossRef]
37. USDA. Chapter 9: Hydrological Soil-Cover Complexes. In *USDA National Engineering Handbook*; USDA: Washington, DC, USA, 2004. Available online: https://directives.sc.egov.usda.gov/viewerfs.aspx?hid=21422 (accessed on 9 May 2023).
38. Hong, Y.; Adler, R.F. Estimation of Global SCS Curve Numbers Using Satellite Remote Sensing and Geospatial Data. *Int. J. Remote Sens.* **2008**, *29*, 471–477. [CrossRef]
39. Hoeft, C.C. Incorporating Updated Runoff Curve Number Technology into NRCS Directives. In *Watershed Management 2020: A Clear Vision of Watershed Management*; ASCE: Reston, VA, USA, 2020; pp. 78–87. [CrossRef]
40. Akan, A.O. Horton Infiltration Equation Revisited. *J. Irrig. Drain. Eng.* **1992**, *118*, 828–830. [CrossRef]
41. Rawls, W.J.; Brakensiek, D.L.; Miller, N. Green-ampt Infiltration Parameters from Soils Data. *J. Hydraul. Eng.* **1983**, *109*, 62–70. [CrossRef]
42. Dahak, A.; Boutaghane, H.; Merabtene, T. Parameter Estimation and Assessment of Infiltration Models for Madjez Ressoul Catchment, Algeria. *Water* **2022**, *14*, 1185. [CrossRef]
43. Miyata, S.; Gomi, T.; Sidle, R.C.; Onda, Y.; Yamamoto, K.; Nonoda, T.; Hiraoka, M.; Kosugi, K. Evaluation of Spatial Patterns of Infiltration Capacity on Storm Runoff in a Forested Watershed: Utilizing of LiDAR Data in a Distributed Runoff Model. In Proceedings of the American Geophysical Union Fall Meeting, San Francisco, CA, USA, 15–19 December 2008.
44. Langhans, C.; Govers, G.; Diels, J.; Leys, A.; Clymans, W.; den Putte, A.V.; Valckx, J. Experimental Rainfall–Runoff Data: Reconsidering the Concept of Infiltration Capacity. *J. Hydrol.* **2011**, *399*, 255–262. [CrossRef]
45. Nuottimäki, K.; Jarva, J. A Qualitative Approach for Identifying Areas Prone to Urban Floods with the Support of LiDAR. *GFF* **2015**, *137*, 373–382. [CrossRef]
46. McGuire, L.A.; Rengers, F.K.; Kean, J.W.; Staley, D.M.; Mirus, B.B. Incorporating Spatially Heterogeneous Infiltration Capacity into Hydrologic Models with Applications for Simulating Post-Wildfire Debris Flow Initiation. *Hydrol. Process.* **2018**, *32*, 1173–1187. [CrossRef]
47. Miyata, S.; Gomi, T.; Sidle, R.C.; Hiraoka, M.; Onda, Y.; Yamamoto, K.; Nonoda, T. Assessing Spatially Distributed Infiltration Capacity to Evaluate Storm Runoff in Forested Catchments: Implications for Hydrological Connectivity. *Sci. Total Environ.* **2019**, *669*, 148–159. [CrossRef]
48. Roca, D.; Armesto, J.; Lagüela, S.; Díaz-Vilariño, L. Lidar-Equipped Uav for Building Information Modelling. *Int. Arch. Photogramm. Remote Sens. Spat. Inf. Sci.* **2014**, *XL-5*, 523–527. [CrossRef]
49. Luo, H.; Wang, L.; Wu, C.; Zhang, L. An Improved Method for Impervious Surface Mapping Incorporating LiDAR Data and High-Resolution Imagery at Different Acquisition Times. *Remote Sens.* **2018**, *10*, 1349. [CrossRef]
50. Baby, S.N.; Arrowsmith, C.; Liu, G.-J.; Mitchell, D.; Al-Ansari, N.; Abbas, N. Finding Areas at Risk from Floods in a Downpour Using the Lidar-Based Elevation Model. *J. Civ. Eng. Archit.* **2021**, *15*, 1–16. Available online: https://www.researchgate.net/publication/349098888_Finding_Areas_at_Risk_from_Floods_in_a_Downpour_Using_the_Lidar-Based_Elevation_Model (accessed on 30 May 2023).
51. Chapa, F.; Hariharan, S.; Hack, J. A New Approach to High-Resolution Urban Land Use Classification Using Open Access Software and True Color Satellite Images. *Sustainability* **2019**, *11*, 5266. [CrossRef]
52. Qu, L.; Chen, Z.; Li, M.; Zhi, J.; Wang, H. Accuracy Improvements to Pixel-Based and Object-Based Lulc Classification with Auxiliary Datasets from Google Earth Engine. *Remote Sens.* **2021**, *13*, 453. [CrossRef]
53. Khosravi, K.; Pham, B.T.; Chapi, K.; Shirzadi, A.; Shahabi, H.; Revhaug, I.; Prakash, I.; Tien Bui, D. A Comparative Assessment of Decision Trees Algorithms for Flash Flood Susceptibility Modeling at Haraz Watershed, Northern Iran. *Sci. Total Environ.* **2018**, *627*, 744–755. [CrossRef]

54. Khosravi, K.; Shahabi, H.; Pham, B.T.; Adamowski, J.; Shirzadi, A.; Pradhan, B.; Dou, J.; Ly, H.-B.; Gróf, G.; Ho, H.L.; et al. A Comparative Assessment of Flood Susceptibility Modeling Using Multi-Criteria Decision-Making Analysis and Machine Learning Methods. *J. Hydrol.* **2019**, *573*, 311–323. [CrossRef]
55. Wang, Y.; Hong, H.; Chen, W.; Li, S.; Pamučar, D.; Gigović, L.; Drobnjak, S.; Tien Bui, D.; Duan, H. A Hybrid GIS Multi-Criteria Decision-Making Method for Flood Susceptibility Mapping at Shangyou, China. *Remote Sens.* **2019**, *11*, 62. [CrossRef]
56. Gudiyangada Nachappa, T.; Tavakkoli Piralilou, S.; Gholamnia, K.; Ghorbanzadeh, O.; Rahmati, O.; Blaschke, T. Flood Susceptibility Mapping with Machine Learning, Multi-Criteria Decision Analysis and Ensemble Using Dempster Shafer Theory. *J. Hydrol.* **2020**, *590*, 125275. [CrossRef]
57. Birch, G.F.; Fazeli, M.S.; Matthai, C. Efficiency of an infiltration basin in removing contaminants from urban stormwater. *Env. Monit Assess* **2005**, *101*, 23–38. [CrossRef]
58. Widomski, M.K.; Sobczuk, H.; Olszta, W. Sand-Filled Drainage Ditches for Erosion Control: Effects on Infiltration Efficiency. *Soil Sci. Soc. Am. J.* **2010**, *74*, 213–220. [CrossRef]
59. De Carlo, L.; Caputo, M.C.; Masciale, R.; Vurro, M.; Portoghese, I. Monitoring the Drainage Efficiency of Infiltration Trenches in Fractured and Karstified Limestone via Time-Lapse Hydrogeophysical Approach. *Water* **2020**, *12*, 2009. [CrossRef]
60. Archer, N.A.L.; Bell, R.A.; Butcher, A.S.; Bricker, S.H. Infiltration Efficiency and Subsurface Water Processes of a Sustainable Drainage System and Consequences to Flood Management. *J. Flood Risk Manag.* **2020**, *13*, e12629. [CrossRef]
61. Državni Zavod Za Statistiku. Popis '21. Available online: https://popis2021.hr/ (accessed on 30 March 2022).
62. Docs&Tools—STREAM—Italia-Croatia. Available online: https://programming14-20.italy-croatia.eu/web/stream/docs-and-tools (accessed on 23 October 2023).
63. Galić, J. Regionalizacija Donjoneretvanske Delte. *Naše More Znan. Časopis Za More I Pomor.* **2011**, *58*, 39–46.
64. Šiljković, Ž.; Glamuzina, M. Mogućnost Uvođenja Eko–Poljoprivrede u Deltu Neretve. *Soc. Ekol. Časopis Za Ekološku Misao I Sociol. Istraživanja Okoline* **1999**, *8*, 183–191.
65. DHMZ Croatian Meteorological and Hydrological Service. *Climate Atlas of Croatia 1961–1990, 1971–2000*; DHMZ: Zagreb, Croatia, 2008. Available online: https://klima.hr/razno/publikacije/klimatski_atlas_hrvatske.pdf (accessed on 30 May 2023).
66. Discover Trinity F90+. The Unbeatable Mapping Drone. Available online: https://quantum-systems.com/trinity-f90/ (accessed on 30 May 2023).
67. Comparison of MicaSense Cameras. Available online: https://support.micasense.com/hc/en-us/articles/1500007828482-Comparison-of-MicaSense-Cameras (accessed on 30 May 2023).
68. Maté-González, M.Á.; Di Pietra, V.; Piras, M. Evaluation of Different LiDAR Technologies for the Documentation of Forgotten Cultural Heritage under Forest Environments. *Sensors* **2022**, *22*, 6314. [CrossRef]
69. Alphonse, A.B.; Wawrzyniak, T.; Osuch, M.; Hanselmann, N. Applying UAV-Based Remote Sensing Observation Products in High Arctic Catchments in SW Spitsbergen. *Remote Sens.* **2023**, *15*, 934. [CrossRef]
70. Mitka, B.; Klapa, P.; Pióro, P. Acquisition and Processing Data from UAVs in the Process of Generating 3D Models for Solar Potential Analysis. *Remote Sens.* **2023**, *15*, 1498. [CrossRef]
71. Zenmuse L1. UAV Load Gimbal Camera—DJI Enterprise. Available online: https://enterprise.dji.com/photo (accessed on 16 May 2023).
72. Dearden, R.A.; Marchant, A.; Royse, K. Development of a Suitability Map for Infiltration Sustainable Drainage Systems (SuDS). *Env. Earth Sci.* **2013**, *70*, 2587–2602. [CrossRef]
73. Blaschke, T. Object Based Image Analysis for Remote Sensing. *ISPRS J. Photogramm. Remote Sens.* **2010**, *65*, 2–16. [CrossRef]
74. MacFaden, S.W.; O'Neil-Dunne, J.P.M.; Royar, A.R.; Lu, J.W.T.; Rundle, A.G. High-Resolution Tree Canopy Mapping for New York City Using LIDAR and Object-Based Image Analysis. *J. Appl. Remote Sens.* **2012**, *6*, 063567. [CrossRef]
75. Hay, G.J.; Castilla, G. Geographic Object-Based Image Analysis (GEOBIA): A New Name for a New Discipline. In *Object-Based Image Analysis: Spatial Concepts for Knowledge-Driven Remote Sensing Applications*; Blaschke, T., Lang, S., Hay, G.J., Eds.; Lecture Notes in Geoinformation and Cartography; Springer: Berlin/Heidelberg, Germany, 2008; pp. 75–89, ISBN 978-3-540-77058-9.
76. Lang, S. Object-Based Image Analysis for Remote Sensing Applications: Modeling Reality—Dealing with Complexity. In *Object-Based Image Analysis*; Springer: Berlin/Heidelberg, Germany, 2008. Available online: https://link.springer.com/book/10.1007/978-3-540-77058-9 (accessed on 12 April 2023).
77. Comaniciu, D.; Meer, P. Mean Shift: A Robust Approach toward Feature Space Analysis. *IEEE Trans. Pattern Anal. Mach. Intell.* **2002**, *24*, 603–619. [CrossRef]
78. Millard, K.; Richardson, M. On the Importance of Training Data Sample Selection in Random Forest Image Classification: A Case Study in Peatland Ecosystem Mapping. *Remote Sens.* **2015**, *7*, 8489–8515. [CrossRef]
79. Ye, S.; Pontius, R.G.; Rakshit, R. A Review of Accuracy Assessment for Object-Based Image Analysis: From per-Pixel to per-Polygon Approaches. *ISPRS J. Photogramm. Remote Sens.* **2018**, *141*, 137–147. [CrossRef]
80. Dixon, B.; Candade, N. Multispectral Landuse Classification Using Neural Networks and Support Vector Machines: One or the Other, or Both? *Int. J. Remote Sens.* **2008**, *29*, 1185–1206. [CrossRef]
81. Gibril, M.B.A.; Bakar, S.A.; Yao, K.; Idrees, M.O.; Pradhan, B. Fusion of RADARSAT-2 and Multispectral Optical Remote Sensing Data for LULC Extraction in a Tropical Agricultural Area. *Geocarto Int.* **2017**, *32*, 735–748. [CrossRef]

82. Fragou, S.; Kalogeropoulos, K.; Stathopoulos, N.; Louka, P.; Srivastava, P.K.; Karpouzas, S.; Kalivas, D.P.; Petropoulos, G.P. Quantifying Land Cover Changes in a Mediterranean Environment Using Landsat TM and Support Vector Machines. *Forests* **2020**, *11*, 750. [CrossRef]
83. Oo, T.K.; Arunrat, N.; Sereenonchai, S.; Ussawarujikulchai, A.; Chareonwong, U.; Nutmagul, W. Comparing Four Machine Learning Algorithms for Land Cover Classification in Gold Mining: A Case Study of Kyaukpahto Gold Mine, Northern Myanmar. *Sustainability* **2022**, *14*, 10754. [CrossRef]
84. Train Support Vector Machine Classifier (Spatial Analyst)—ArcMap | Documentation. Available online: https://desktop.arcgis.com/en/arcmap/latest/tools/spatial-analyst-toolbox/train-support-vector-machine-classifier.htm (accessed on 17 August 2023).
85. Congalton, R.G. A Review of Assessing the Accuracy of Classifications of Remotely Sensed Data. *Remote Sens. Environ.* **1991**, *37*, 35–46. [CrossRef]
86. Liu, C.; Frazier, P.; Kumar, L. Comparative Assessment of the Measures of Thematic Classification Accuracy. *Remote Sens. Environ.* **2007**, *107*, 606–616. [CrossRef]
87. Thompson, W.D.; Walter, S.D. A Reappraisal of the Kappa Coefficient. *J. Clin. Epidemiol.* **1988**, *41*, 949–958. [CrossRef]
88. Rigby, A.S. Statistical Methods in Epidemiology. v. Towards an Understanding of the Kappa Coefficient. *Disabil. Rehabil.* **2000**, *22*, 339–344. [CrossRef] [PubMed]
89. Koukoulas, S.; Blackburn, G.A. Mapping Individual Tree Location, Height and Species in Broadleaved Deciduous Forest Using Airborne LIDAR and Multi-spectral Remotely Sensed Data. *Int. J. Remote Sens.* **2005**, *26*, 431–455. [CrossRef]
90. Šiljeg, A.; Panđa, L.; Domazetović, F.; Marić, I.; Gašparović, M.; Borisov, M.; Milošević, R. Comparative Assessment of Pixel and Object-Based Approaches for Mapping of Olive Tree Crowns Based on UAV Multispectral Imagery. *Remote Sens.* **2022**, *14*, 757. [CrossRef]
91. Kou, X.; Han, D.; Cao, Y.; Shang, H.; Li, H.; Zhang, X.; Yang, M. Acid Mine Drainage Discrimination Using Very High Resolution Imagery Obtained by Unmanned Aerial Vehicle in a Stone Coal Mining Area. *Water* **2023**, *15*, 1613. [CrossRef]
92. Park, G.; Park, K.; Song, B.; Lee, H. Analyzing Impact of Types of UAV-Derived Images on the Object-Based Classification of Land Cover in an Urban Area. *Drones* **2022**, *6*, 71. [CrossRef]
93. Jozdani, S.E.; Johnson, B.A.; Chen, D. Comparing Deep Neural Networks, Ensemble Classifiers, and Support Vector Machine Algorithms for Object-Based Urban Land Use/Land Cover Classification. *Remote Sens.* **2019**, *11*, 1713. [CrossRef]
94. Lu, D.; Weng, Q. A Survey of Image Classification Methods and Techniques for Improving Classification Performance. *Int. J. Remote Sens.* **2007**, *28*, 823–870. [CrossRef]
95. Abdullah, A.Y.M.; Masrur, A.; Adnan, M.S.G.; Baky, M.A.A.; Hassan, Q.K.; Dewan, A. Spatio-Temporal Patterns of Land Use/Land Cover Change in the Heterogeneous Coastal Region of Bangladesh between 1990 and 2017. *Remote Sens.* **2019**, *11*, 790. [CrossRef]
96. Wardlow, B.D.; Egbert, S.L. Large-Area Crop Mapping Using Time-Series MODIS 250 m NDVI Data: An Assessment for the US Central Great Plains. *Remote Sens. Environ.* **2008**, *112*, 1096–1116. [CrossRef]
97. Malinverni, E.S.; Tassetti, A.N.; Mancini, A.; Zingaretti, P.; Frontoni, E.; Bernardini, A. Hybrid Object-Based Approach for Land Use/Land Cover Mapping Using High Spatial Resolution Imagery. *Int. J. Geogr. Inf. Sci.* **2011**, *25*, 1025–1043. [CrossRef]
98. Rajendran, G.B.; Kumarasamy, U.M.; Zarro, C.; Divakarachari, P.B.; Ullo, S.L. Land-Use and Land-Cover Classification Using a Human Group-Based Particle Swarm Optimization Algorithm with an LSTM Classifier on Hybrid Pre-Processing Remote-Sensing Images. *Remote Sens.* **2020**, *12*, 4135. [CrossRef]
99. Radočaj, D.; Jurišić, M.; Gašparović, M. The Role of Remote Sensing Data and Methods in a Modern Approach to Fertilization in Precision Agriculture. *Remote Sens.* **2022**, *14*, 778. [CrossRef]
100. Vidaček, Ž.; Bogunović, M.; Husnjak, S.; Sraka, M.; Bensa, A. Hydropedological Map of the Republic of Croatia. *Agric. Conspec. Sci.* **2008**, *73*, 67–74.
101. Gitelson, A.A.; Kaufman, Y.J.; Merzlyak, M.N. Use of a Green Channel in Remote Sensing of Global Vegetation from EOS- MODIS. *Remote Sens. Environ.* **1996**, *58*, 289–298. [CrossRef]
102. Patón, D. Normalized Difference Vegetation Index Determination in Urban Areas by Full-Spectrum Photography. *Ecologies* **2020**, *1*, 22–35. [CrossRef]
103. Huang, S.; Tang, L.; Hupy, J.P.; Wang, Y.; Shao, G. A Commentary Review on the Use of Normalized Difference Vegetation Index (NDVI) in the Era of Popular Remote Sensing. *J. For. Res.* **2021**, *32*, 1–6, Erratum in *J. For. Res.* **2021**, *32*, 2719. [CrossRef]
104. Braun, M.; Herold, M. Mapping Imperviousness Using NDVI and Linear Spectral Unmixing of ASTER Data in the Cologne-Bonn Region (Germany). In Proceedings of the Remote Sensing for Environmental Monitoring, GIS Applications, and Geology III, Barcelona, Spain, 8–12 September 2003; SPIE: Paris, France, 2004; Volume 5239, pp. 274–284.
105. Zhang, Y.; Odeh, I.O.; Han, C. Bi-Temporal Characterization of Land Surface Temperature in Relation to Impervious Surface Area, NDVI and NDBI, Using a Sub-Pixel Image Analysis. *Int. J. Appl. Earth Obs. Geoinf.* **2009**, *11*, 256–264. [CrossRef]
106. Knight, J.; Voth, M. Mapping Impervious Cover Using Multi-Temporal MODIS NDVI Data. *IEEE J. Sel. Top. Appl. Earth Obs. Remote Sens.* **2010**, *4*, 303–309. [CrossRef]
107. Guo, W.; Lu, D.; Wu, Y.; Zhang, J. Mapping Impervious Surface Distribution with Integration of SNNP VIIRS-DNB and MODIS NDVI Data. *Remote Sens.* **2015**, *7*, 12459–12477. [CrossRef]

108. Guo, W.; Lu, D.; Kuang, W. Improving Fractional Impervious Surface Mapping Performance through Combination of DMSP-OLS and MODIS NDVI Data. *Remote Sens.* **2017**, *9*, 375. [CrossRef]
109. Rouse, J.W.; Haas, R.H.; Schell, J.A.; Deering, D.W. Monitoring Vegetation Systems in the Great Plains with ERTS. *NASA Spec. Publ.* **1974**, *351*, 309.
110. Morbidelli, R.; Saltalippi, C.; Flammini, A.; Govindaraju, R.S. Role of Slope on Infiltration: A Review. *J. Hydrol.* **2018**, *557*, 878–886. [CrossRef]
111. Yu, H.; Zhao, Y.; Fu, Y. Optimization of Impervious Surface Space Layout for Prevention of Urban Rainstorm Waterlogging: A Case Study of Guangzhou, China. *Int. J. Environ. Res. Public Health* **2019**, *16*, 3613. [CrossRef]
112. Sytsma, A.; Bell, C.; Eisenstein, W.; Hogue, T.; Kondolf, G.M. A Geospatial Approach for Estimating Hydrological Connectivity of Impervious Surfaces. *J. Hydrol.* **2020**, *591*, 125545. [CrossRef]
113. Meierdiercks, K.L.; Kolozsvary, M.B.; Rhoads, K.P.; Golden, M.; McCloskey, N.F. The Role of Land Surface versus Drainage Network Characteristics in Controlling Water Quality and Quantity in a Small Urban Watershed. *Hydrol. Process.* **2017**, *31*, 4384–4397. [CrossRef]
114. Sugianto, S.; Deli, A.; Miswar, E.; Rusdi, M.; Irham, M. The Effect of Land Use and Land Cover Changes on Flood Occurrence in Teunom Watershed, Aceh Jaya. *Land* **2022**, *11*, 1271. [CrossRef]
115. Różycka, M.; Migoń, P.; Michniewicz, A. Topographic Wetness Index and Terrain Ruggedness Index in Geomorphic Characterisation of Landslide Terrains, on Examples from the Sudetes, SW Poland. *Z. Für Geomorphol. Suppl. Issues* **2016**, *61*, 61–80. [CrossRef]
116. Raduła, M.W.; Szymura, T.H.; Szymura, M. Topographic Wetness Index Explains Soil Moisture Better than Bioindication with Ellenberg's Indicator Values—ScienceDirect. Available online: https://www.sciencedirect.com/science/article/abs/pii/S1470160X17306350 (accessed on 30 May 2023).
117. Jaynes, D.B. Temperature Variations Effect on Field-Measured Infiltration. *Soil Sci. Soc. Am. J.* **1990**, *54*, 305–312. [CrossRef]
118. Braga, A.; Horst, M.; Traver, R.G. Temperature Effects on the Infiltration Rate through an Infiltration Basin BMP. *J. Irrig. Drain. Eng.* **2007**, *133*, 593–601. [CrossRef]
119. Malczewski, J.; Rinner, C. (Eds.) Introduction to GIS-MCDA. In *Multicriteria Decision Analysis in Geographic Information Science*; Advances in Geographic Information Science; Springer: Berlin/Heidelberg, Germany, 2015; pp. 23–54, ISBN 978-3-540-74757-4.
120. Fuzzy Membership (Spatial Analyst)—ArcMap | Documentation. Available online: https://desktop.arcgis.com/en/arcmap/latest/tools/spatial-analyst-toolbox/fuzzy-membership.htm (accessed on 25 February 2023).
121. Pamučar, D.; Stević, Ž.; Sremac, S. A New Model for Determining Weight Coefficients of Criteria in MCDM Models: Full Consistency Method (FUCOM). *Symmetry* **2018**, *10*, 393. [CrossRef]
122. Németh, B.; Molnár, A.; Bozóki, S.; Wijaya, K.; Inotai, A.; Campbell, J.D.; Kaló, Z. Comparison of Weighting Methods Used in Multicriteria Decision Analysis Frameworks in Healthcare with Focus on Low- and Middle-Income Countries. *J. Comp. Eff. Res.* **2019**, *8*, 195–204. [CrossRef] [PubMed]
123. Ishizaka, A.; Labib, A. Review of the Main Developments in the Analytic Hierarchy Process. *Expert Syst. Appl.* **2011**, *38*, 14336–14345. [CrossRef]
124. Sałabun, W.; Ziemba, P.; Wątróbski, J. The Rank Reversals Paradox in Management Decisions: The Comparison of the AHP and COMET Methods. In Proceedings of the Intelligent Decision Technologies 2016, Puerto de la Cruz, Spain, 15–17 June 2016; Czarnowski, I., Caballero, A.M., Howlett, R.J., Jain, L.C., Eds.; Springer International Publishing: Cham, Switzerland, 2016; pp. 181–191.
125. Domazetović, F.; Šiljeg, A.; Lončar, N.; Marić, I. GIS Automated Multicriteria Analysis (GAMA) Method for Susceptibility Modelling. *MethodsX* **2019**, *6*, 2553–2561. [CrossRef]
126. Shawky, M.; Hassan, Q.K. Geospatial Modeling Based-Multi-Criteria Decision-Making for Flash Flood Susceptibility Zonation in an Arid Area. *Remote Sens.* **2023**, *15*, 2561. [CrossRef]
127. Saaty, T.L. What Is the Analytic Hierarchy Process? In *Mathematical Models for Decision Support*; Mitra, G., Greenberg, H.J., Lootsma, F.A., Rijkaert, M.J., Zimmermann, H.J., Eds.; Springer: Berlin/Heidelberg, Germany, 1988; pp. 109–121.
128. Solano, F.; Di Fazio, S.; Modica, G. A Methodology Based on GEOBIA and WorldView-3 Imagery to Derive Vegetation Indices at Tree Crown Detail in Olive Orchards. *Int. J. Appl. Earth Obs. Geoinf.* **2019**, *83*, 101912. [CrossRef]
129. Panđa, L.; Milošević, R.; Šiljeg, S.; Domazetović, F.; Marić, I.; Šiljeg, A. Comparison of GEOBIA classification algorithms based on Worldview-3 imagery in the extraction of coastal coniferous forest. *Šumar. List Online* **2021**, *145*, 535–544. [CrossRef]
130. Šiljeg, A.; Marinović, R.; Domazetović, F.; Jurišić, M.; Marić, I.; Panđa, L.; Radocaj, D.; Milošević, R. GEOBIA and Vegetation Indices in Extracting Olive Tree Canopies Based on Very High-Resolution UAV Multispectral Imagery. *Appl. Sci.* **2023**, *13*, 739. [CrossRef]
131. Manandhar, R.; Odeh, I.O.A.; Ancev, T. Improving the Accuracy of Land Use and Land Cover Classification of Landsat Data Using Post-Classification Enhancement. *Remote Sens.* **2009**, *1*, 330–344. [CrossRef]
132. Ardila, J.P.; Tolpekin, V.A.; Bijker, W.; Stein, A. Markov-Random-Field-Based Super-Resolution Mapping for Identification of Urban Trees in VHR Images. *ISPRS J. Photogramm. Remote Sens.* **2011**, *66*, 762–775. [CrossRef]
133. Dihkan, M.; Guneroglu, N.; Karsli, F.; Guneroglu, A. Remote Sensing of Tea Plantations Using an SVM Classifier and Pattern-Based Accuracy Assessment Technique. *Int. J. Remote Sens.* **2013**, *34*, 8549–8565. [CrossRef]

134. Panđa, L. Imperviousness Density Mapping Based on GIS-MCDA and High-Resolution Worldview-2 Imagery. In Proceedings of the 9th International Conference on Geographical Information Systems Theory, Applications and Management (GISTAM 2023), Lisbon, Portugal, 25–27 April 2023; p. 229. Available online: https://www.scitepress.org/Link.aspx?doi=10.5220/0011988200003473 (accessed on 25 February 2023).
135. Dong, X.; Meng, Z.; Wang, Y.; Zhang, Y.; Sun, H.; Wang, Q. Monitoring Spatiotemporal Changes of Impervious Surfaces in Beijing City Using Random Forest Algorithm and Textural Features. *Remote Sens.* **2021**, *13*, 153. [CrossRef]
136. Shrestha, B.; Stephen, H.; Ahmad, S. Impervious Surfaces Mapping at City Scale by Fusion of Radar and Optical Data through a Random Forest Classifier. *Remote Sens.* **2021**, *13*, 3040. [CrossRef]
137. Shrestha, B.; Ahmad, S.; Stephen, H. Fusion of Sentinel-1 and Sentinel-2 Data in Mapping the Impervious Surfaces at City Scale. *Environ. Monit. Assess.* **2021**, *193*, 556. [CrossRef] [PubMed]
138. Lin, J.; Zhang, W.; Wen, Y.; Qiu, S. Evaluating the Association between Morphological Characteristics of Urban Land and Pluvial Floods Using Machine Learning Methods. *Sustain. Cities Soc.* **2023**, *99*, 104891. [CrossRef]
139. Slonecker, E.T.; Jennings, D.B.; Garofalo, D. Remote Sensing of Impervious Surfaces: A Review. *Remote Sens. Rev.* **2001**, *20*, 227–255. [CrossRef]
140. Baldinelli, G.; Bonafoni, S.; Anniballe, R.; Presciutti, A.; Gioli, B.; Magliulo, V. Spaceborne Detection of Roof and Impervious Surface Albedo: Potentialities and Comparison with Airborne Thermography Measurements. *Sol. Energy* **2015**, *113*, 281–294. [CrossRef]
141. Lee, K.; Lee, W.H. Temperature Accuracy Analysis by Land Cover According to the Angle of the Thermal Infrared Imaging Camera for Unmanned Aerial Vehicles. *ISPRS Int. J. Geo-Inf.* **2022**, *11*, 204. [CrossRef]
142. Lee, S.; Moon, H.; Choi, Y.; Yoon, D.K. Analyzing Thermal Characteristics of Urban Streets Using a Thermal Imaging Camera: A Case Study on Commercial Streets in Seoul, Korea. *Sustainability* **2018**, *10*, 519. [CrossRef]
143. Cho, H. Effects of Road Components and Roadside Vegetation on Temperature Reduction in Seoul Considering Air, Wet-Bulb Globe, and Surface Temperatures. *Sustainability* **2022**, *14*, 16663. [CrossRef]
144. Morabito, M.; Crisci, A.; Guerri, G.; Messeri, A.; Congedo, L.; Munafò, M. Surface Urban Heat Islands in Italian Metropolitan Cities: Tree Cover and Impervious Surface Influences. *Sci. Total Environ.* **2021**, *751*, 142334. [CrossRef] [PubMed]

Disclaimer/Publisher's Note: The statements, opinions and data contained in all publications are solely those of the individual author(s) and contributor(s) and not of MDPI and/or the editor(s). MDPI and/or the editor(s) disclaim responsibility for any injury to people or property resulting from any ideas, methods, instructions or products referred to in the content.